Article DOI: https://doi.org/10.1016/j.orggeochem.2020.104174

Temperature and water depth effects on brGDGT distributions in sub-alpine lakes of mid-latitude North America

Ioana C. Stefanescu[a,*], Bryan N. Shuman[a], Jessica E. Tierney[b]

a Department of Geology and Geophysics, University of Wyoming, Laramie, WY, USA

b Department of Geosciences, University of Arizona, Tucson, AZ, USA

*Corresponding author at: Department of Geology and Geophysics, University of Wyoming, Laramie, WY 82071, USA

E-mail address: istefane@uwyo.edu (I.C. Stefanescu)

Keywords: lake sediments, 5- and 6-methyl brGDGTs, temperature calibration, mid-latitude

Abstract

Branched glycerol dialkyl glycerol tetraethers (brGDGTs) in lake sediments are increasingly being used to reconstruct past temperatures. However, recent studies suggest that brGDGT distributions and concentrations vary with lake size and environmental conditions such as seasonality and its effects on water column temperature and chemistry. To test their use as a paleothermometer in high-altitude environments of mid-latitude North America, we analyzed brGDGT distributions in lake surface sediments across a range of lake depths and elevations in the Rocky Mountains of Wyoming and Colorado. Our results suggest that brGDGT distributions and the MBT'5Me index correlate with water column temperatures, which are sensitive to both lake water depth and air temperatures. Based on these relationships, we developed a calibration to mean summer air temperatures using a Bayesian regression model that incorporates the MBT'_{5Me} index and lake water depth. We applied our calibration to lake sediments from Lower Paintrock Lake in northern Wyoming to test its use as a paleothermometer. Reconstructed temperature trends are consistent with pollen-inferred temperatures at the same site and with known regional climate history, demonstrating that our calibration can be successfully applied to infer temperatures in high-altitude environments of mid-latitude North America.

1. Introduction

Lacustrine branched glycerol dialkyl glycerol tetraethers (brGDGTs) are increasingly being used to reconstruct past mean annual air temperatures (MAAT) based on their abundances in sediment sequences [Loomis et al., 2012, Loomis et at., 2015, Miller et al., 2018, Ning et al., 2019, Feng et al., 2019]. Branched GDGTs are membrane-spanning lipids thought to be produced by bacteria living in soils, peats, freshwater and marine environments across the globe [Schouten et al., 2000, Sinninghe Damsté et al., 2000, Peterse et al., 2009, Peterse et al., 2012, De Jonge et al., 2014a, Sinninghe Damsté 2016]. The compounds were initially presumed to be synthesized by bacteria living in soils and transported to lakes and rivers via erosion [Hopmans et al., 2004], but subsequent studies found evidence that brGDGTs are being produced in the water column or in aquatic sediments [Tierney and Russell, 2009, 2010; Bechtel et al., 2010; Zhu et al., 2011; Loomis et al., 2012; Schoon et al., 2013; Zell et al., 2013, Miller et al., 2018, Martínez-Sosa and Tierney 2019]. However, the exact species of bacteria producing these compounds is still unknown [Weijers et al., 2009; Sinninghe Damsté, 2018].

The brGDGTs compounds have a core structure comprised of two ether-linked dialkyl chains [Weijers et al., 2006], with a differing number of methyl groups (4, 5, or 6) and cyclopentane rings (0, 1, or 2) [Weijers et al., 2007; De Jonge et al., 2013, 2014a]. Weijers et al., (2007) showed that the degree of methylation (the number of tetra-, penta-, or hexa-methylated brGDGTs with 4, 5, or 6 methyl groups, respectively) is related to mean annual temperatures while the degree of cyclization (the number of cyclopentane rings) is related to pH; they then defined a temperature-sensitive index of the methylation of branched tetraethers (MBT) as the

ratio of the summed abundance of tetra-methylated compounds to the summed abundance of all brGDGTs and a pH-sensitive index of the cyclization of branched tetraethers (CBT) as the ratio between the sum of the most abundant cyclic compounds to the sum of the non-cyclic compounds.

Recent improvements in chromatographic separation led to the identification of isomers with methyl group positions at position ω/α5 or at position ω/α6, also referred to as 5-methyl and 6-methyl isomers [De Jonge et al., 2013, 2014a; Hopmans et al., 2016]. De Jonge et al., [2013, 2014a, 2014b] showed that the removal of 6-methyl isomers from the methylation index improves temperature calibrations. The new methylation index, MBT'_{5Me}, excludes the 6-methyl isomers [De Jonge et al., 2013] and has been calibrated to MAAT using global soil datasets [De Jonge et al., 2014b, Naafs et al., 2017b, Crampton-Flood et al., 2020], a lacustrine dataset from East Africa [Russell et al., 2018] and a global peat dataset [Naafs et al., 2017a.] However, brGDGT distributions in sediments of small, snow-fed lakes of cold mid-latitude, high-elevation settings analogous to the high latitudes have not been extensively examined.

Temperature reconstructions in cold, high-altitude environments such as the Rocky Mountain region of mid-latitude North America have been challenging to produce. Commonly used paleothermometers, such as $\delta^{18}O$ of lake carbonates, can be hard to interpret because multiple environmental factors such as the seasonality of precipitation and evapotranspiration influence the results [Leng and Marshall, 2004]. Fossil pollen has been widely used for paleothermometry in mid- to high-latitude regions [Marsicek et al., 2018], but testing ecological hypotheses related to climate change requires independent lines of evidence and some key species in the

79 Rocky Mountain region, in particular, have broad temperature tolerances that limit
80 their utility [Minckley et al., 2012]. Therefore, an independent temperature proxy
81 such as brGDGTs is needed to evaluate the temperature history of this region.

82 Previous studies suggest that brGDGT distributions may be seasonally
83 biased towards late summer or fall in temperate regions [Buckles et al., 2014a,
84 Loomis et al., 2014a, Miller et al., 2018, Dang et al., 2018] and that their
85 concentration increases with increasing water depth [Sinninghe Damsté et al., 2009,
86 Buckles et al., 2014a, Miller et al., 2018]. However, the relatively short summer
87 season in high-elevation, cold environments of mid-latitude North America where
88 snow and ice cover persist from early November to late June [Musselman, 1994,
89 Liefert et al., 2018] can potentially influence the seasonality of lacustrine production
90 of brGDGTs [Cao et al., 2020]. Given these considerations, the existing MBT'_{5Me}
91 calibration for lakes in East Africa may not be universally applicable [Russell et al.,
92 2018].

93 Here we present 5- and 6-methyl brGDGT distributions in modern sediments
94 from 34 small sub-alpine lakes in the Rocky Mountains of Wyoming and Colorado.
95 The lakes vary in elevation, mean annual air temperature, mean summer air
96 temperature, summer water temperature, degree of stratification (i.e., surface versus
97 bottom temperature differences), and water depth (Table 1). Our results indicate
98 that the bacteria synthesizing these compounds are sensitive to summer lake water
99 column temperatures, which depend upon interactions of air temperature and lake
100 depth. Based on these results, we develop a regional calibration to summer air
101 temperatures using a Bayesian regression model that incorporates both mean
102 summer air temperature and water depth as predictors for the methylation index

103 (MBT'_{5Me}). We then apply the calibration to lake sediments spanning the last 14 kyr
104 from Lower Paintrock Lake in northern Wyoming to test its use as a
105 paleothermometer.

106 ## 2. Methods

107 ### 2.1 Study sites

108 We collected modern surface sediments from 34 lakes located in northern
109 Colorado and Wyoming (Fig. 1). Of these, 21 lakes were sampled in the Medicine
110 Bow Mountains, southern Wyoming, during July-September 2017 when these lakes
111 experience maximum water temperatures [Musselman 1994, Liefert et al., 2018].
112 We also incorporated samples previously collected from three lakes in the Bighorn
113 and Beartooth Mountains in northern Wyoming [Shuman and Serravezza, 2017] and
114 ten additional samples from lakes in the nearby Park Range, Colorado, collected
115 during the summers between 2010 and 2016 [Calder et al., 2015]. They expand our
116 dataset, but do not have accompanying water temperature data. Two of the northern
117 lakes (Duncan and Rainbow Lakes) were sampled at different water depths [Shuman
118 and Serravezza, 2017] and Round Lake (southern WY) was sampled twice in 2017
119 at similar water depths, which enabled intra-lake comparisons of brGDGTs. Duncan
120 Lake was sampled at depths of 0.95, 1.16 and 1.78 m, Rainbow Lake was sampled at
121 depths of 1, 1.4, and 2.5 m, and Round Lake was sampled twice at a constant depth
122 of 1.2m. Altogether, we analyzed 39 surface sediment samples.

123 All samples were collected in polycarbonate core tubes lowered by hand
124 either using coring rods or rope, and the upper 1 cm of sediment was preserved for
125 analysis. Summer water column temperatures were measured at 17 lakes in the

126 Medicine Bow Mountains (Table 1) while dissolved oxygen concentrations and pH
127 were measured at 16 of these lakes (Supplementary Table 1). Mean annual air and
128 mean summer air temperature data for each lake was obtained using the Parameter-
129 Elevation Regressions on Independent Slopes Model (PRISM) with a resolution of
130 800 meters from the Climate Group at Oregon State University [Prism Climate
131 Group, 2018]. Mean annual air temperature (MAAT) was calculated using 30-year
132 averages (1981-2010) and mean summer air temperature (JJAS) was calculated by
133 averaging the 30-year monthly averages of June, July, August and September.

134 We use JJAS as a representative air temperature in the statistical
135 comparisons because our lake water temperature measurements also represent
136 summer conditions. Our results are interchangeable whether we use MAAT or JJAS
137 because both correlate with elevation in our calibration dataset (Table 2) and we do
138 not have statistical power to separate one from the other. Our use of JJAS is
139 consistent, however, with previous work. Lacustrine and soil brGDGT distributions
140 in mid-latitude, temperate regions are seasonally biased towards late summer or fall
141 [Buckles et al., 2014a, Loomis et al., 2014a, Miller et al., 2018, Dang et al., 2018;
142 Crampton-Flood et al. 2020]. Our lakes also remain frozen for most of the year
143 (October to early June) and, during the ice-cover season, lake water temperatures
144 remain near 4 °C while air temperatures can drop well below 4 °C [Musselman
145 1994; Liefert et al., 2018; see also Cao et al., 2020].

146 A sediment core from Lower Paintrock Lake, Wyoming (44.390 N, 107.380°
147 W, 2808 m elevation), collected using a hand-driven piston corer with 70 mm
148 polycarbonate tubes, was used to test the application of the brGDGT analyses (Fig.
149 1, diamond). Lower Paintrock Lake (LPR) is a small moraine-dammed lake

surrounded by dense lodgepole pine (*Pinus contorta*) forest, dry sagebrush (*Artemisia* spp.) meadows, and riparian areas dominated by willow (*Salix* spp.). Lily pads (*Nuphar polysepala*) grow in shallow areas of the lake, which formed in an area of Archean gneiss, quartz diorite, and quartz monzonite behind the Pinedale-age (Last Glacial Maximum) terminal moraines at the head of Paintrock Creek [Green and Drouillard, 1994]. Fossil pollen provide a record of vegetation changes at the site, which include modest shifts in the relative abundances of the conifer tree taxa during the Holocene (Rust and Minckley, 2020). Streams flow into and out of the lake, which has an area of 9.38 ha and a maximum depth of 5.8 meters. MAAT and JJAS at LPR equal 0.6 and 10°C respectively (Table 1).

The 4.63 m core from LPR was obtained at a water depth of 5.7 m near the center of the lake and was subsampled at 1 cm increments. Sub-samples were sealed in sterile whirl-pak bags and stored at 4 °C. We analyzed 36 samples for brGDGT distributions at intervals of ~11.5cm (sampling interval mean: 11.5 cm, std: 5.4 cm). The age model was derived from 12 radiocarbon dates (Supplementary Table 2) calibrated to calendar years using the *bchron* package in R (Supplementary Fig. 1), which models sediment accumulation based on a Bayesian model accounting of the radiocarbon ages using the INTCAL 13 calibration curve [Parnell et al., 2008]. For this study, we accounted for the rate of sediment deposition to infer the Holocene change in water depth at LPR (Fig. 9).

2.2 BrGDGT analysis

Lipids were extracted from 2-8 g of freeze-dried sediment using an Accelerated Solvent Extractor (ASE Dionex 350) at the University of Wyoming with dichloromethane: methanol (9:1, volume:volume, hereafter v:v). The total lipid

extract was separated over an aminopropyl (LC-NH2) solid phase column using DCM: Isopropanol (2:1, v:v) then re-dissolved in Hexane and separated over silica gel columns using Hexane, DCM and MeOH to isolate the aliphatic hydrocarbon, ketone, and polar fractions respectively. The polar fraction, containing the GDGTs, was re-dissolved in Hexane:Isopropanol (99:1, v:v) and filtered through 0.45 μm polytetrafluoroethylene filters prior to analysis. BrGDGT analyses were performed using the methodology of Hopmans et al., [2016] on an Agilent 6210 single quadrupole mass spectrometer coupled to a 1260/1290 Infinity high-performance liquid chromatograph and fitted with two BEH HILIC silica columns (2.1 x 150 mm, 1.7 μm, Waters) at the University of Arizona. To assess instrumental precision, 37% of the samples were analyzed in duplicate. Average duplicate standard deviation was 0.001 for the MBT'$_{5Me}$ index. Peaks were identified manually based on comparison with the C46 internal standard (Huguet et al., 2006) and integrated automatically using the ORganIc Geochemistry peAk Integration package [Fleming and Tierney, 2016].

2.3 Mathematical analysis and notations

The individual brGDGT compounds are symbolized with the prefixes I, II and III representing compounds with 4, 5 or 6 methyl groups, respectively (also referred to as tetra-, penta- and hexa-methylated compounds) and are followed by the suffixes a, b, or c representing 0, 1 and 2 cyclopentane rings, respectively. Isomers are represented using the same nomenclature, but with a prime variant to designate the 6-methyl isomers (').

Fractional abundance f(i) of each brGDGT compound (i) is defined as follows and includes both 5- and 6-methyl isomers:

$$f(i) = i / (Ia+Ib+Ic+IIa+IIa'+IIb+IIb'+IIc+IIc'+IIIa+IIIa'+IIIb+IIIb'+IIIc+IIIc')$$

where i varies from Ia, Ib, etc, as mentioned above. Accordingly, the fractional abundances of tetra-, penta- and hexa-methylated compounds are defined as the ratio of the summed individual abundances of a-c compounds (including isomers for each group of compounds: I, II and III) to the summed abundances of all compounds.

The MBT'_{5Me} and CBT' indices were calculated as in De Jonge et al. [2014a]:

$$MBT'_{5Me} = (Ia + Ib + Ic) / (Ia + Ib + Ic + IIa + IIb + IIc + IIIa)$$

$$CBT' = \log_{10}[(Ic + IIa' + IIb' + IIc' + IIIa' + IIIb' + IIIc') / (Ia + IIa + IIIa)]$$

All of our statistical treatments of the data were completed using base functions in R and MATLAB [R Core Team, 2018, The MathWorks, Inc.]. To account for uncertainties in each of our calibration model parameters (air temperature, water depth and MBT'_{5Me}), we chose a Bayesian approach as in Tierney and Tingley [2014], Tierney et al. [2019] and Crampton-Flood et al. [2020]. The Bayesian regression model is fully described in Crampton-Flood et al. [2020].

To infer the regression parameters between the MBT'_{5Me} index and the environmental predictor variables, we use a model of the form:

$$Y = X\beta + \varepsilon$$

$$\varepsilon \sim N(0,\sigma^2)$$

where Y is a n-length vector of MBT'_{5Me} values with n as the number of samples. X is a n x E+1 matrix containing corresponding values of E number of environmental predictor variables and a vector of ones to represent the intercept. β is a vector of E+1 length containing the regression parameters, while ε (n-length vector) is a normally distributed error term centered around zero with variance σ^2.

Pollen-inferred temperatures at Lower Paintrock Lake were reconstructed using pollen data from Rust and Minckley [2020] and the methods of Parish et al., [2020]. The cross-correlation function (CCF) between the brGDGT- and pollen-inferred JJAS reconstructions was calculated by accounting for serial autocorrelation and uneven sample spacing using the BINCOR package in R [Polanco-Martinez et al., 2019].

3. Results

3.1 Relationships among modern environmental variables

Our dataset contains lake surface sediments from 34 small alpine lakes (<20 ha) which range from 0.5 to 25 m in depth, -0.8 to 2.6 °C in mean annual air temperature (hereafter MAAT), 8.2 to 12 °C in mean summer temperature (JJAS), and from 2701 to 3350 m in elevation (Table 1). Water column temperatures were measured at 17 of these lakes across a similar range of water depth and environmental temperatures; they showed that summer lake surface temperatures (T_{SURF}) range from 12.2 to 20.6 °C and summer lake bottom temperatures (T_{BOT}) range from 4.2 to 20.1 °C. Lakes shallower than 7 meters are well mixed in late summer with an average temperature difference of 1.6 °C between surface and

240 bottom waters while lakes deeper than 7 meters show an average temperature
241 difference of 7.2 °C.

242 We analyzed correlations among environmental variables that may control
243 the local water temperatures (Table 2). First, both MAAT and JJAS at each lake
244 correlated with elevation. T_{SURF} also showed a similar correlation with both
245 elevation, MAAT and JJAS. The relationships extended further to T_{BOT}, which
246 correlate with T_{SURF}, elevation, MAAT and JJAS. However, water depth also
247 mediates and correlates with both T_{SURF} and T_{BOT}. The average water column
248 temperatures also strongly correlate with T_{SURF}, T_{BOT}, MAAT, JJAS, water depth and
249 elevation. No significant correlation was found between water depth and elevation,
250 MAAT or JJAS.

251 We measured water column dissolved oxygen concentrations (DO) and pH at
252 16 of the lakes where water temperatures were also recorded (water depths range
253 from 0.5 to 16.2 m; Supplementary Table 1). DO in surface waters (DO_{SURF}) range
254 from 5.6 to 8.7 mg/L and from 0.01 to 12.1 mg/L in bottom waters (DO_{BOT}). Anoxic
255 conditions (DOC< 1mg/L) were found in the bottom waters of four lakes with water
256 depths >7m, low DO of 3.2 and 3.7 mg/L waters were found in bottom waters of
257 two lakes (water depths of 16.2 and 9.9 m, respectively), while all other lakes had
258 well oxygenated waters throughout the water column with a DO range of 5.2-12.1
259 mg/L. The pH of the surface waters (pH_{SURF}) ranges from 6.8-9.6 and from 6.0 to 9.7
260 in bottom waters (pH_{BOT}) suggesting that most of our lakes are alkaline.

261 We analyzed correlations among environmental variables that may influence
262 DO (Table 2) and found a strong positive correlation between DO_{BOT} and T_{BOT} and a
263 strong negative correlation between DO_{BOT} and water depth. Furthermore, DO_{BOT}

also correlates with T_{SURF} and average water temperatures. No statistically significant correlations were found between DO_{SURF} and DO_{BOT} or between DO_{SURF} and any of the environmental variables (Table 2). DO_{BOT} is also significantly correlated to $pH_{BOT,}$ which further correlates with water depth, MAAT, JJAS, average water temperature, T_{BOT} and elevation. The pH_{TOP} shows no significant correlation to any of the environmental variables (Table 2).

3.2 BrGDGT analysis of modern lake sediment

The brGDGT compounds with the highest fractional abundances in the lake surface sediment samples (Fig. 2a) are: (1) compound IIIa with a mean of 0.26 (σ = 0.09), (2) compound IIa with a mean of 0.26 (σ = 0.05) and (3) compound Ia with a mean of 0.18 (σ = 0.06). This relative abundance pattern of increasing fractional abundance with increasing methylation for the 5-methyl isomers of the non-cyclic brGDGTs (Ia<IIa<IIIa) is most evident in sediment samples collected at water depths >3m (Fig. 2b). Conversely, in sediment samples collected at water depths <3 m, compound IIIa displays a lower fractional abundance as compared to IIa and Ia (Fig. 2c). Although some samples had low concentrations of bicyclic brGDGT compounds (IIc, IIc', IIIc and IIIc'), we achieved full separation of 5- and 6-methyl brGDGTs in all lake surface sediments as well as in the down core samples from LPR. Abundances were too low for compound IIc to be reliably quantified in 5% of the samples, for compound IIc' in 25% of the samples, for compound IIIc in 57% of the samples and for compound IIIc' in 67% of the samples.

The resulting MBT'_{5Me} values range from 0.10 to 0.40 with a mean of 0.27 and σ = 0.08 across lake surface sediment samples (Fig. 3, Table 1). We found a negative relationship between water depth and the MBT'_{5Me} index (Spearman

correlation =-0.83, $p<0.001$) where lakes sampled at water depths <3m show higher MBT'_{5Me} values than lakes sampled at water depths >3m (Fig. 3, Table 3). At constant sampling depth (e.g., at a depth of 6 m in Fig. 3), the MBT'_{5Me} values are a function of elevation.

We compared the grouped fractional abundances of tetra-, penta- and hexa-methylated compounds with JJAS, T_{SURF}, and T_{BOT} for 17 surface sediment samples where these variables were measured (Fig. 4). T_{BOT} best explains the variations of all three grouped fractional abundances including tetra-methylated compounds (Spearman's r=0.83; $p<0.001$), penta-methylated compounds (Spearman's r=0.68; p=0.003) and hexa-methylated compounds (Spearman's r=-0.79; $p<0.001$). JJAS and T_{SURF} show statistically significant correlations with the summed fractional abundances of tetra- and hexa-methylated compounds (Fig. 4a,b) and no statistically significant correlations with penta-methylated compounds (p-values of 0.089 and 0.128, respectively). Moreover, the fractional abundances of the grouped tetra- and penta-methylated compounds show a positive relationship to JJAS, T_{SURF}, and T_{BOT}, and a negative relationship to water depth (Fig. 4, colored palette). Conversely, the fractional abundances of the grouped hexa-methylated compounds show a negative relationship to JJAS, T_{SURF}, and T_{BOT}, and a positive relationship to water depth (Fig. 4, colored palette).

The elevation and water depth influence on the MBT'_{5Me} index are also observed in sediment samples collected at different water depths within individual lakes (Fig. 5). MBT'_{5Me} values are higher by an average of 0.11 in sediments collected at Duncan Lake (elev. 2800m) versus Rainbow Lake (elev. 3000m), while the MBT'_{5Me} index of intra-lake sediment samples is inversely related to water

depth. MBT'$_{5Me}$ values at Duncan Lake decrease by an average of 0.07 between sediments collected at 1, 1.5 and 2 m depth. In comparison, MBT'$_{5Me}$ values at Rainbow Lake decrease by an average of 0.02 between sediments collected at 1, 1.5 and 2.5 m depth. Furthermore, samples collected at the same water depth (Round Lake, depths of 1.2 m) exhibit an insignificant difference in MBT'$_{5Me}$.

We also compared the grouped fractional abundances of tetra-, penta- and hexa-methylated compounds with the DO_{BOT} for the 16 surface sediment samples where DO was measured. DO_{BOT} is positively correlated to the MBT'$_{5Me}$ index (Table 3), to the grouped tetra-methylated compounds (Spearman's r=0.59; p=0.018) and penta-methylated compounds (Spearman's r=0.65; p=0.008) and negatively correlated to the grouped hexa-methylated compounds (Spearman's r=-0.68; p=0.005). No significant correlations were found between DO_{SURF} and any of the grouped fractional abundances or the MBT'$_{5Me}$ index (Spearman's $r<0.16$, $p>0.05$). Even though DO_{BOT} correlates with the grouped fractional abundances and with the MBT'$_{5Me}$ index, a multivariate linear regression model that includes DO_{BOT} and T_{BOT} as predictors for the MBT'$_{5Me}$ index shows that DO_{BOT} is not a significant predictor for the MBT'$_{5Me}$ index (regression coefficient on DO_{BOT}=0.0006, p=0.915).

We find that surface and bottom water pH are not significantly correlated to the CBT' index (Table 3). Furthermore, except for a significant correlation between bottom water pH and the fractional abundance of compound IIIa (Spearman's r=-0.70, p=0.004), no significant correlations were found between surface or bottom water pH and the fractional abundance of any of the other individual 5- and 6-methyl compounds.

As with the individual groups of compounds (Fig. 4), we regressed the MBT'$_{5Me}$ index against JJAS, T_{SURF}, and T_{BOT} for all lakes as well as just shallow or deep lakes (Fig. 6). Consistent with the other results, shallow lakes exhibit much higher MBT'$_{5Me}$ values than deep lakes; significantly distinct regression lines were calculated for shallow and deep lakes (Fig. 6, dashed lines). If water depth is excluded (Fig. 6, black solid lines), the strongest relationship is found between the MBT'$_{5Me}$ index and T_{BOT} (Fig. 6c: adjusted r^2=0.63, $p<0.001$, n=17; all depths). However, only weak relationships are found between the MBT'$_{5Me}$ index and JJAS or T_{SURF} when we do not account for water depth (Fig. 6a,b black solid lines: adjusted r^2 = 0.03 and 0.31, respectively).

3.3 BrGDGT calibration to summer lake bottom temperatures

Summer lake bottom temperatures (T_{BOT}) integrate influences of both water depth and JJAS and show a strong relationship to the MBT'$_{5Me}$ index at the 17 of lakes where we measured T_{BOT} (Fig. 6c). A Bayesian regression model fit to the MBT'$_{5Me}$ data with T_{BOT} as the predictor indicates a significant relationship:

$$MBT'_{5Me} = 0.015\ (\pm 0.003) * T_{BOT}(°C) + 0.07(\pm 0.04)$$

and error σ^2=0.003 (±0.001)

where the coefficients and their uncertainties represent the mean and one standard deviation of 4500 iterations of possible slope, intercept and error values generated by the Bayesian regression model.

To predict T_{BOT} from MBT'$_{5Me}$ values, we invert the calibrated relationship between MBT'$_{5Me}$ and T_{BOT}. This step requires a prior mean on T_{BOT} which we set as the mean of T_{BOT} at our sites (11.5°C) and a prior standard deviation, which we set to

two times the standard deviation of T_{BOT} at our sites (2σ=9.2 °C) to ensure a range of variance suitable for the expected predictions.

The observed versus predicted values of T_{BOT} plot along the 1:1 reference line (Fig. 7) with no trend in the residuals (Spearman's r=-0.24, p=0.357). The RMSE of predicted T_{BOT} is 2.8 °C. None of the points were identified as statistical outliers, but two of the samples (East Glacier and Hourglass lakes, Fig. 7) represent large departures from the mean relationship.

3.4 Calibration of brGDGTs to summer air temperatures

T_{BOT} is correlated with JJAS and water depth and multivariate linear model (T_{BOT} = JJAS + ln(water depth)) indicates a significant relationship (adjusted r^2=0.74, p<0.001). Therefore, we also developed a Bayesian model to calibrate MBT'_{5Me} to JJAS by accounting for water depth. We use log-transformed water depth as a predictor variable because the relationship between water depth and the MBT'_{5Me} index is nonlinear (Fig. 3).

The Bayesian calibration model for MBT'_{5Me} as a function of both summer air temperature (JJAS) and ln(water depth) at mid-latitude, high-elevation North America is:

MBT'_{5Me}= 0.026 (± 0.007) * JJAS °C - 0.065 (± 0.007) * ln(water depth in meters) + 0.10 (± 0.07)

and error σ^2=0.002 (±0.0005)

where the coefficients and their uncertainties represent the mean and one standard deviation of 4500 iterations of possible slope, intercept and error values generated by the Bayesian regression model.

The observed versus predicted values of MBT'_{5Me} plot along the 1:1 reference line (Fig. 8a). However, residuals in the relationship (Fig. 8a) retain a correlation that might suggest the importance of an additional unconstrained variable (Spearman's r=-0.41, p=0.01).

To predict JJAS from MBT'_{5Me} values and ln(water depth) values, we invert the relationship between MBT'_{5Me}, JJAS, and ln(water depth). The prior mean and standard deviation on JJAS was set to the mean of JJAS at our sites (10 °C) with a large standard deviation (5 °C) to ensure a range of variance suitable for the expected predictions.

The observed versus predicted values of JJAS plot along the 1:1 reference line (Fig. 8b) with no trend in the residuals (Spearman's r=-0.12, p=0.459). The RMSE of predicted JJAS is 1.3 °C. We also inverted the Bayesian model to predict ln(water depth) to assess the model performance. The observed versus predicted values of ln(water depth) also plot along the 1:1 reference line (Fig. 8c) with no trend in the residuals (Spearman's r=-0.18, p=0.263). The RMSE of predicted ln(water depth) is 0.62 (or 1.9 m). LPR plots on the 1:1 lines of observed versus predicted MBT'_{5ME}, JJAS and ln(WD) (Figure 8, red points), which indicates the applicability of the model to downcore reconstructions from LPR.

For comparison, we also applied the previously published calibration for MAAT based on lake surface sediments from East Africa [Russell et al., 2018] to

our MBT'$_{5Me}$ results, but the inferred temperatures of 2.0 to 12.9 °C overestimate MAAT at our lakes (Table 1). Similarly, the existing calibration for mean April-October temperatures for cold regions from lakes in China [Dang et al., 2018] reconstructed temperatures with an unreasonable range of -7.3 to 13.4 °C (Table 1).

3.5 BrGDGT analysis of downcore sediment at Lower Paintrock Lake, WY

The brGDGT compounds with the highest fractional abundances in the downcore sediment samples are: (1) compound IIa with a mean of 0.25 ($\sigma = 0.05$), (2) compound IIIa with a mean of 0.22 ($\sigma = 0.05$) and (3) compound Ia with a mean of 0.22 ($\sigma = 0.05$). The MBT'$_{5Me}$ values range from 0.21 to 0.41 (Supplementary Table 3) with a mean of 0.32 ($\sigma = 0.05$). Abundances were too low for compound IIc' to be reliably quantified in 14% of the samples and for compound IIIc' in 50% of the samples in the downcore sediment from LPR.

3.6 Application of the JJAS and T_{BOT} calibrations at Lower Paintrock Lake, WY

The Holocene trend in reconstructed summer air temperatures inferred from the brGDGTs at LPR (Fig. 9c, black line; Supplementary Table 3) is broadly consistent with that inferred from pollen at the same site (Figure 9c, orange line). However, the absolute temperatures differ. The latest Holocene brGDGT sample (i.e., core top) indicates a JJAS temperature 2.4 °C cooler than inferred from the pollen, although the modern JJAS predicted by PRISM for LPR (10 °C, Table 1) falls within the uncertainty of both reconstructions (Fig. 9c). By contrast, the mean JJAS inferred from Holocene brGDGTs samples older than 1000 B.P. equals 14 °C, which is 2.8 °C warmer than the mean JJAS inferred from the pollen for the same

period (Fig. 9c). The two timeseries correlate significantly when the upper two samples have been excluded from the brGDGT reconstruction (cross correlation function, CCF; $r_{x,y}$ =0.624 at 95% C.I., lag=0), but the inclusion of the top samples reduces the correlation ($r_{x,y}$ =0.283 at 95% C.I., lag=0). No significant CCF correlations were found at other lags. Because JJAS and MAAT co-vary across Rocky Mountain calibration sample sets for both pollen and brGDGTs, an alternative model based on MAAT also yields a reconstruction consistent with the pollen data; Supplementary Fig. 2, Supplementary Table 4).

The brGDGTs reconstruct JJAS trends consistent with the pollen-inferred reconstruction and the known forcings despite the absolute temperature offset (Figure 9a,c). The record indicates warming from 14 ka to mid-Holocene (ΔT=3.9 °C; Fig. 9a) consistent with the regional climate effects of the retreat of the Laurentide Ice Sheet (LIS) [Dyke A. 2004]. A subsequent cooling trend persists until present (ΔT=4.6 °C) consistent with decreasing summer insolation anomalies in the northern hemisphere (Fig. 9a) [Berger and Loutre, 1991]. We focus on the long-term trends because of the low temporal sampling resolution and age uncertainties, but additional millennial variability is also present in the record including during the mid- and late-Holocene. Both the brGDGTs and pollen indicate Holocene temperature maxima at ca. 8 and 5.5 ka (Fig. 9c).

The difference between the brGDGT and pollen-inferred JJAS reconstructions in the youngest samples parallels another unexpected pattern in the brGDGT- derived JJAS reconstruction, which yields temperatures for the late-Pleistocene that are 3.1 °C higher than indicated by our most recent samples (Fig. 9c, black line). During the cold Younger Dryas interval (12.7-11.6 ka), reconstructed

JJAS temperatures are 1.8 °C higher than estimated from the core top samples (Fig. 9c).

If we reconstruct lake bottom temperatures instead of air temperatures for the Holocene from LPR (Fig. 9b), the reconstruction falls within the range of lake bottom temperatures observed today during the summer at our other sites (Table 1). If the data are interpreted to represent T_{BOT} instead of JJAS, then the reconstruction indicates a similar long-term pattern with a warming trend from 14 ka to mid-Holocene (ΔT=7.6 °C) followed by a subsequent cooling trend until present (ΔT=10.5 °C). As with the JJAS reconstruction, the T_{BOT} reconstruction also yields lower-than-Pleistocene temperatures for the most recent samples (Fig. 9b).

4. Discussion

4.1 Lacustrine BrGDGTs and temperatures in mid-latitude mountain ranges

Previous analyses using brGDGT distributions suggest a relationship to MAAT in regions with limited temperature seasonality or when the dataset covers a wide geographical region with a large range of MAATs [Russell et al., 2018; Dang et al., 2018]. However, our study represents a region with substantial temperature seasonality that spans a small range of MAAT (-0.9 to 2.6 °C) and JJAS (8.2 to 12 °C). We also include many samples from shallow lakes like those commonly studied in mid-to-high latitudes. We detect correlations of brGDGT distributions to elevation, related air temperatures, and water column temperatures, but at our sites, we find that air temperatures (either MAAT or JJAS) alone cannot explain the variations in the MBT'_{5Me} index; therefore, existing lacustrine brGDGT calibrations

to MAAT [Russell et al., 2018] or to growing season air temperatures [Dang et. al., 2018] do not work well at our sites (Table 1).

Instead, our results emphasize linkages to warm season temperatures and water temperatures at depth within our study lakes (Fig. 6) suggesting in situ production. The relationships appear consistent with those of Cao et al. [2020], who proposed that brGDGT distributions track mean annual lake water temperatures, but that warm-season air temperatures strongly control these values in mid- and high-latitudes lakes. Their lake water temperature model for mid-latitudes suggest that winter ice cover decouples lake water temperatures from air temperatures as water temperatures remain constant at ~4 °C even though air temperatures drop far below 0 °C. In contrast, the model shows that lake water temperatures during the ice-free season closely track air temperatures and therefore, the mean annual lake water temperatures are biased towards the warm season. Since MAAT and JJAS at our sites are significantly correlated, we do not have statistical power to distinguish seasonality, but our results affirm a strong relationship to water temperatures (Table 2). The Cao et al., [2020] lake water temperature model could explain the strong correlation we find between the brGDGT distributions and lake water temperatures during the summer. If so, brGDGT distributions may change both as the length and maximum warmth of the ice-free season changes and some differences between the brGDGT- and pollen-inferred temperature histories at LPR may have resulted from such effects.

For the small and shallow lakes from our geographically confined study area, a relationship to water depth is also apparent and appears to modulate the

493 temperature response (Figures 3-6). Below, we consider the source of this influence
494 before evaluating our Bayesian model for inferred JJAS.

495 4.2 Influence of water depth

496 The distribution of lacustrine brGDGTs in sub-alpine environments of mid-
497 latitude North America appears sensitive to both water depth and summer air
498 temperatures (Fig. 6). The water depth is particularly significant where water depth
499 decreases below 3 m (Fig. 6). Water depth influences both the fractional abundances
500 (Fig. 2) and the MBT'$_{5Me}$ index (Fig. 3) with different relationships to temperature
501 apparent in shallow (<3m) versus deep lakes (>3m) (Fig. 6). At a given elevation
502 (and JJAS), shallow lakes exhibit higher fractional abundances of tetra-methylated
503 compounds than deep lakes, which exhibit high abundances of hexa-methylated
504 compounds (Fig. 2). Consequently, the MBT'$_{5Me}$ index decreases with increasing
505 water depth and helps to explain the scatter in the relationships of JJAS (varying
506 across elevations in Fig. 3) to individual groups of brGDGTs (Fig. 4) or the MBT'$_{5Me}$
507 index (Fig. 6). The MBT'$_{5Me}$ index exhibits similar negative relationships to water
508 depth across sites (Fig. 3) and among samples from different water depths within
509 individual lakes (Fig. 5). The consistency suggests localized influences on the suite
510 of compounds whether through in-situ production or differences in delivery of
511 terrestrial compounds. However, the differences with depth within individual lakes
512 clarify that the effect is not related to length of the ice-free season nor some other
513 factor intrinsic to shallow versus deep lakes.

514 Our results differ from those of Dang et al., [2018], who found no
515 relationship between water depth and the MBT'$_{5Me}$ index, even though their study
516 includes sites with similar water depths. This dissimilarity could be due to the fact

517 that the sites studied by Dang et al., [2018] span a wide range of MAATs (-0.2 to
518 17.2 °C), which may mask the relationship between water depth and the MBT'$_{5Me}$
519 index because water column temperatures are a function of both water depth and air
520 temperatures. In contrast, our sites span a relatively small range of MAATs (-0.8 to
521 2.6 °C) and JJAS (8.2 to 12 °C), but a relatively broad range of water depths (0.5-25
522 m) and T_{BOT} (4.2 to 20.1 °C), which allowed us to examine the effect of water depth
523 on lacustrine brGDGT distributions. We also have a large proportion of samples
524 from <3 m water depth. Additionally, the samples examined by Dang et al., [2018]
525 have a lower fractional abundance of compound IIIa (μ =0.06, σ =0.02) than our
526 (μ=0.26, σ=0.09) or than Russell et all., [2018] (μ=0.16, σ=0.16). The difference
527 could result in different water depth-MBT'$_{5Me}$ relationships. Compound IIIa can
528 weigh heavily on the MBT'$_{5Me}$ index and exhibits a strong water-depth signature
529 (Fig. 2). We speculate that differences in bacterial communities or different
530 environmental conditions such as salinity or high alkalinity could have caused the
531 distinct fractional abundance distributions observed by Dang et al., [2018].

532 As small and shallow waterbodies dominate terrestrial environments at a
533 global scale [Downing et al., 2006], the potential influence of lake depth on
534 brGDGT distributions in these settings needs to be considered. Similar findings were
535 also reported at a relatively shallow (10m deep) Gonghai Lake situated in the mid-
536 latitudes of China where the methylation index decreases with water depth in
537 suspended particulate matter samples (SPM) as well as in the sediments [Cao et al.,
538 2020]. Furthermore, Cao et al. [2020] also reported an increase in the brGDGT
539 content with increasing water depth and hypothesized that brGDGTs are likely being
540 produced in situ, at depth in the water column. Our data also suggests that depth

plays a more important role in shallow lakes and that the influence of depth on brGDGTs distributions weakens as water depth increases (Fig. 3).

We find no significant correlations between pH and the CBT' index or individual brGDGT compounds except for compound IIIa, which is significantly correlated with pH_{BOT}. Since compound IIIa is corelated to other environmental variables such as water depth, DO, T_{BOT} and MAAT, we cannot tease apart the influence of pH_{BOT} on brGDGT distributions. However, we note that other studies have found pH to have a relatively weak influence on lacustrine brGDGT distributions [Tierney et al., 2010; Loomis et al., 2014b; Russell et al., 2018].

4.3 Examining the relationship to water temperatures

At our sites, different JJAS-MBT'_{5Me} relationships for lakes of different depths converge to a single relationship once T_{BOT} is considered (Fig. 6), which is a function of both lake water depth and air temperatures during the summer. During summer months, the shallow lakes are well mixed and exhibit small differences between top and bottom water temperatures (average $\Delta T = 0.2$ °C); bottom water temperatures reach temperatures as high as 20.1 °C because the whole body of well mixed waters interacts with the atmosphere. In contrast, bottom waters in deep lakes remain cool below the thermocline. The difference in mixing explains the larger range of lake bottom temperatures (4.2-20.1 °C) compared to the associated MAATs at the same sites (-0.8 to 2.2 °C) or JJAS temperatures (8.2 to 12 °C) and helps to explain the range of fractional abundances and MBT'_{5Me} values (Fig. 6).

T_{BOT} exhibits the strongest relationships to both fractional abundance of all grouped compounds (Fig. 4) and to the MBT'_{5Me} index (Fig. 6). The result could

suggest that brGDGTs are preferentially synthesized in situ by bacteria at depth in the water column. However, multiple alternative hypotheses could explain the strong MBT'$_{5Me}$ relationship to T_{BOT}: bacteria may produce brGDGTs (1) only at depth in the water column, 2) across the full range of different temperatures and redox conditions in the complete water column, providing an integrated signal correlated with the range of T_{BOT}, including preferential production of certain compounds in different portions of the water column (e.g., hexa-methylated compounds in the hypolimnion), (3) in lake sediments, or (4) in situ, but the compounds mix in shallow water near-shore with those washed in from adjacent soils.

The various correlations within our dataset can help to evaluate the different hypotheses. For example, because average water column temperatures strongly correlate with T_{BOT}, brGDGT production throughout the water column could be tracking an integrated lake water column temperature signal. The grouped fractional abundances display the strongest correlations to T_{BOT} (Fig. 4), but the grouped tetra-methylated compounds are also significantly correlated to T_{SURF} (Spearman's r=0.68, p=0.003). The correlation between the tetra-methylated compounds and T_{SURF} could be the result of the correlation between T_{BOT} and T_{SURF}, but some fraction of the tetra-methylated compounds may be produced in surface waters. We, therefore, cannot attribute the range of brGDGT distributions at our sites solely to brGDGT production in bottom waters. This observation agrees with previous sediment trap studies that show that even though brGDGT concentrations are higher at depth in the water column than in the surface waters during thermal stratification, brGDGT production takes place throughout the water column [Loomis et al., 2014b; Buckles et al., 2014b; Miller et al., 2018]. Our correlations might be misleading, however,

588 because single measurements of T_{BOT} may be more representative of average lake
589 conditions during the summer than the highly variable T_{SURF}.

590 Additional factors other than temperature may also drive production at depth
591 in the water column. Bacteria synthesizing hexa-methylated compounds could prefer
592 the cool environments of bottom waters for reasons other than temperature and
593 therefore produce patterns in the MBT'$_{5Me}$ index associated with bottom water
594 temperatures. Weber et al. [2018] showed that different redox conditions favor the
595 production of different individual compounds and that the concentration of
596 compound IIIa increases below the redox zone (in the hypolimnion). However,
597 many of our lakes are well mixed. Measured DO at 16 of our lakes suggests that
598 most of these lakes are well oxygenated throughout the water column as bottom
599 water anoxia was found only in four of the lakes (Supplementary Table 1).
600 Moreover, the fractional abundance of hexa-methylated compounds and the
601 MBT'$_{5Me}$ index suggest a weaker relationship to DO_{BOT} than to T_{BOT}. Multiple
602 regression indicates no statistically significant linear dependence of the MBT'$_{5Me}$
603 index on DO_{BOT} when both DO_{BOT} and T_{BOT} are included in the model. Since anoxia
604 was not found in all 16 lakes where DO was measured and, DO is not the best
605 explanatory variable for compound IIIa, we speculate that, at our sites, compound
606 IIIa is not being produced solely in anoxic waters. Instead, the decrease in the
607 MBT'$_{5Me}$ index with increasing water depth (associated with high abundances of
608 compound IIIa) suggests that bacteria living below the thermocline or in deep waters
609 are producing more hexa-methylated compounds due to a decrease in water column
610 temperatures and not due to anoxic waters. We cannot exclude the possibility that
611 either some or all of the compounds are also being produced in the sediments
612 [Tierney et al., 2012]. Even though sediment temperatures were not measured at our

613 sites, we suspect that they would reflect T_{BOT} and would produce similar correlations
614 to the MBT'$_{5Me}$ index. However, our dataset limits us from testing this hypothesis.
615 Finally, the lack of soil data at our sites prohibits us from directly investigating the
616 possibility that brGDGTs could also be washed into the lakes from adjacent soils,
617 but the high abundance of hexa-methylated compounds, in particular compound IIIa
618 (Fig, 2), and the decrease in the MBT'$_{5Me}$ index with depth within individual lakes
619 (Fig. 5) suggests in situ production.

620 In summary, our study shows that lake depth and mixing regime are likely
621 important factors in determining the distribution of brGDGTs in small lakes of mid-
622 latitude North America and that MAAT alone cannot explain the variation in the
623 MBT'$_{5Me}$ index. Instead, brGDGTs at our sites are likely produced in situ and
624 therefore are sensitive to water column temperatures during the summer.
625 Consequently, brGDGTs may be able to be used, especially with water depth
626 information for each sample, to infer JJAS.

627 4.4 MBT'$_{5Me}$ calibration to temperature

628 We can regress T_{BOT} to the MBT'$_{5Me}$ index and reconstruct past T_{BOT} (Fig.
629 7,9), but for paleo-applications, T_{BOT} reconstructions and water depth histories need
630 to be interpreted in tandem as water-depth changes can influence T_{BOT}. In many
631 small lakes, lake-level changes are not inconsequential, even where they only result
632 from sediment infilling (e.g., accumulation of 4.5 m of sediment in 5.7 m of water
633 today at LPR, Fig. 9d). Therefore, calibration to JJAS, which accounts for changes
634 in water depth, may be more useful for understanding past climate changes. Our
635 Bayesian model shows that, if water depth is known, the MBT'$_{5Me}$ index can be used
636 to infer JJAS (Figures 8). We found no trends in the model residuals for JJAS and

637 log-transformed water depth (Fig. 8b,c), which suggests that all deterministic
638 components were captured well by our model.

639 The challenge remains that lake bottom temperatures depend on air
640 temperatures, but also on factors such as lake size, depth, mixing regime, depth of
641 groundwater discharge, and lake morphometry [Almendinger et al., 1990,
642 Rosenberry and LaBaugh 2008]. Rocky Mountain lakes such as those we studied
643 experience lake-specific seasonal temperature trends [Liefert et al., 2018]. Strength
644 of diurnal temperature fluctuations, maximum and minimum summer temperatures,
645 and the magnitude of seasonal temperature changes vary even among lakes of
646 similar size, depth, and location within the watershed. Lake volume can cause
647 substantial differences in seasonal thermal inertia, which depresses maximum water
648 temperatures in large lakes [Liefert et al., 2018]. Groundwater discharge, which has
649 a fairly constant temperature, may also decrease summer lake water temperatures,
650 but varies between lakes and can vary over time altering lake sensitivity to air
651 temperatures [Lee, 1985; Rautio and Korkka-Niemi, 2011; Rosenberry and
652 LaBaugh, 2008]. Because groundwater fluxes in lakes can vary on seasonal and
653 longer time scales [Winter, 1976; Hood et al., 2006] and because thermal
654 stratification isolates the lower portions of the water column, shallow lakes without
655 strong groundwater connections may respond most directly to changes in air
656 temperature through time.

657 Lake-level fluctuations may affect bottom water temperatures in such lakes
658 by influencing the penetration of solar radiation and the degree of mixing, but this
659 effect is not well expressed in many small sub-alpine lakes because the well-mixed
660 water column quickly equilibrates with the atmosphere and observations show

661 limited influence of even >90% reduction in lake volume [Liefert et al., 2018]. The
662 combination of different effects indicates, however, that differences may arise
663 between the inferred lake water temperatures and regional air temperatures,
664 particularly in deep stratified lakes, and need to be considered when interpreting
665 either T_{BOT} or JJAS reconstructions [Dee et al., 2018].

666 4.5 Temperature reconstructions from Lower Paintrock Lake, WY

667 Our brGDGT-based summer air temperature reconstruction from LPR shows
668 Holocene temperatures broadly consistent with the pollen-inferred JJAS
669 reconstruction (Fig. 9c) and other summer temperature reconstructions from the
670 central Rocky Mountains and mid-latitude North America [Whitlock and Bartlein
671 1993; Shuman 2012; Shuman and Marsicek, 2016]. The air temperature trends
672 inferred from both brGDGTs and fossil pollen agree with expected climatic drivers,
673 such as regional warming coincident with the waning regional influence of the
674 Laurentide Ice Sheet (LIS) and subsequent regional cooling driven by declining
675 summer insolation (Fig. 9a). Early in the Holocene when the area and influence of
676 the LIS retained >60% of its LGM extent and continued to exert a large influence on
677 regional climates, summer temperatures were low even though summer insolation
678 exceeded modern. The albedo, topographic, and meltwater effects of the LIS likely
679 kept the northern mid-latitudes cool [Alder et al., 2015]. Temperatures rose steadily
680 as the area and height of LIS declined. As a result, peak Holocene summer air
681 temperatures were only achieved at LPR after ca. 9 ka.

682 Both the brGDGT- and pollen-based reconstructions detect significantly
683 higher than modern temperatures during two maxima between ca. 9-5.5 ka (Fig. 9c).
684 The inferred brGDGT summer air temperature maxima of 16.5 °C at 7.5 ka agrees

685 with the timing of the pollen-inferred maxima of 13.3°C at 7.9 ka. Sub-alpine
686 Wyoming lakes like LPR can reach their maximum summer temperatures in August
687 or September, even though air temperatures peak earlier in the summer [Musselman
688 1994], despite the potential to bias the different reconstructions, the brGDGT-based
689 and pollen-based JJAS trends appear consistent with each other.

690 Our model included the effects of the water-depth changes at LPR inferred
691 by accounting for >4.5 m of sediment deposition during the past 14 kyrs (Fig. 9). In
692 other cases, lake-depth history can be reconstructed using multiple sediment cores to
693 capture common stratigraphic signals produced by lake-level changes [Digerfeldt,
694 1986; Pribyl and Shuman, 2014]. Because LPR remained >5.8 m deep during the
695 Holocene, and the water-depth effect is greatest below 3 m (Fig. 3), water-depth
696 changes had only a minimal influence on the JJAS reconstruction relative to the T_{BOT}
697 reconstruction (Fig. 9). The trends do not differ meaningfully, except in absolute
698 temperature, whether we use the model for T_{BOT} or JJAS (or MAAT). However, the
699 range of temperatures for JJAS and T_{BOT} are different due to the larger range of T_{BOT}
700 compared to the range of JJAS observed at our sites.

701 Unlike the pollen-inferred JJAS, the brGDGT-based temperatures inferred
702 from the core-top samples fall 1.8 °C below even late-Pleistocene temperatures and
703 represent the most enigmatic portion of the record (Fig. 9c). The trends and
704 magnitude of changes in the brGDGT- and pollen-inferred reconstructions appear
705 consistent, but the offsets in the absolute temperature might be consistent with a
706 "cold bias" in the surface samples and calibration dataset. If so, downcore samples
707 may contain a distribution of brGDGTs representative of a warmer environment in
708 the calibration samples that occurred at LPR during the Holocene: a "cold bias" in

surface samples would accurately correlate with modern temperature, but result in a "warm bias" in the reconstruction (i.e., greater fractional abundances of tetra- and penta-methylated compounds and fewer hexa-methylated compounds than expected from surface samples).

The "cold bias" has also been observed in other modern sediment samples [Tierney et al., 2012, Miller et al., 2018]. Possible explanations for the "cold bias" include diagenetic effects on the hexa-methylated compounds or a shift from an oxic lake environment to an anoxic lake environment [Tierney et al., 2012, Weber et al., 2018]. Diagenetic effects on the hexa-methylated compounds would decrease their abundances in older sediments resulting in increased MBT'_{5Me} values down-core. However, no evidence demonstrates different diagenetic effects on compound IIIa relative to other brGDGTs [He et al., 2012]. Although the latter would be surprising here given the history of lake shallowing (Fig. 9d), changes in the seasonal duration or thickness of lake ice cover could be important.

Another possible explanation for the downcore change would be that brGDGTs are produced in the surface sediments in addition to the water column [Tierney and Russell, 2009, 2010; Bechtel et al., 2010; Zhu et al., 2011; Loomis et al., 2012; Schoon et al., 2013; Zell et al., 2013, Miller et al., 2018, Martínez-Sosa and Tierney 2019]. High microbial activity has been shown to extend 10-15 cm into the sediments before declining substantially as energy and oxygen decline [Wurzbacher et al., 2017]. If so, brGDGTs in surface sediments could be biased towards cooler conditions of the sediment-water interface. Overall, some variations in brGDGT abundances may reflect relative changes among different sources whether they are in the water column, watershed or sediments themselves.

733 Based on the difference in brGDGT- reconstructed JJAS between modern
734 sediment samples and the down core sample at ~1 ka (Fig. 9c), our Holocene
735 summer air temperature reconstruction would be offset by +1.9 °C. The offset
736 agrees closely (within 0.5 °C) with the difference between brGDGT- and pollen
737 inferred JJAS in the core top samples (Δ=2.4 °C). More efforts are needed to
738 understand the presence of the "cold bias" in sediment core-tops and future studies
739 could test the existing hypotheses for its occurrence by either: (i) experimentally test
740 the degradation of compound IIIa and identify possible degradation products which
741 could either be isomerization or individual breakdown compounds; or, (ii) use high-
742 resolution sampling of the top of sediment cores to identify where the concentration
743 of compound IIIa attenuates. Moreover, oxic-anoxic environments should be further
744 investigated to better understand the influence of oxygen concentrations on the
745 production of individual brGDGT compounds.

746 5. Conclusion

747 Our study demonstrates that both temperatures and lake water depth
748 influence the relative distributions of 5- and 6-methyl brGDGTs in sub-alpine lakes
749 in mid-latitude North America. Most likely, the influence of depth represents the
750 responsiveness of bacterial lipid composition to changes in water column
751 temperatures, which are a function of both water depth and air temperatures at our
752 sites. The MBT'$_{5Me}$ index correlates well with T_{BOT}, which depends on both air
753 temperatures and water depths, and likely indicates in situ production of brGDGTs
754 within the lake. We show that if water depth is constrained by independent evidence
755 such as sedimentation rate constraints or lake level reconstructions, past air
756 temperatures can be inferred. Our brGDGT-based air temperature reconstruction

757 over the last 14 ka from LPR shows trends consistent with those inferred from fossil
758 pollen and with the known climate forcing for the region including changes in
759 insolation and ice sheet area. Consequently, brGDGTs show promise as a useful
760 paleothermometer at mid-latitude, high-elevation, shallow lakes.

761 Acknowledgements

762 We thank Dr. James Russell and an anonymous reviewer for providing
763 helpful comments that greatly improved our manuscript. We thank P. Murphy for
764 lab analyses and J. Calder, A. Flaim, M. Parish and D. Liefert for assistance with
765 sample collection. This work was supported by the Microbial Ecology Collaborative
766 Project at the University of Wyoming through the National Science Foundation
767 grant EPS-1655726. J. Tierney acknowledges funding support from the National
768 Science Foundation grant EAR-1603674.

769 Data associated with this article is available through the Mountain Scholar
770 database at http://dx.doi.org/10.15786/20.500.11919/7164.

771

772 References

773 Alder, J.R. and Hostetler, S.W., 2015. Global climate simulations at 3000-year
774 intervals for the last 21 000 years with the GENMOM coupled atmosphere-
775 ocean model. Climate of the Past 11, pp. 449–471.

776 Almendinger, J.E., 1990. Groundwater control of closed-basin lake levels under
777 steady-state conditions. Journal of Hydrology 112, pp. 293-318.

778 Bechtel, A., Smittenberg, R.H., Bernasconi, S.M. and Schubert, C.J., 2010.
779 Distribution of branched and isoprenoid tetraether lipids in an oligotrophic
780 and a eutrophic Swiss lake: insights into sources and GDGT-based
781 proxies. Organic Geochemistry 41, pp. 822-832.

782 Berger A. and Loutre M.F., 1991. Insolation values for the climate of the last 10
783 million years. Quaternary Sciences Review 10, pp. 297-317.

784 Buckles, L.K., Weijers, J.W., Verschuren, D. and Damsté, J.S.S., 2014b. Sources of
785 core and intact branched tetraether membrane lipids in the lacustrine
786 environment: Anatomy of Lake Challa and its catchment, equatorial East
787 Africa. Geochimica et Cosmochimica Acta 140, pp. 106-126.

788 Buckles, L.K., Weijers, J.W.H., Tran, X.M., Waldron, S. and Sinninghe Damsté,
789 J.S., 2014a. Provenance of tetraether membrane lipids in a large temperate
790 lake (Loch Lomond, UK): implications for glycerol dialkyl glycerol
791 tetraether (GDGT)-based palaeothermometry. Biogeosciences 11, pp. 5539-
792 5563.

793 Calder, W.J., Parker, D., Stopka, C.J., Jiménez-Moreno, G. and Shuman, B.N.,
794 2015. Medieval warming initiated exceptionally large wildfire outbreaks in
795 the Rocky Mountains. Proceedings of the National Academy of
796 Sciences 112, pp. 13261-13266.

797 Cao, J., Rao, Z., Shi, F. and Jia, G., 2020. Ice formation on lake surfaces in winter
798 causes warm-season bias of lacustrine brGDGT temperature
799 estimates. Biogeosciences 17, pp. 2521-2536.

800 Crampton-Flood, E.D., Tierney, J.E., Peterse, F., Kirkels, F.M. and Damsté, J.S.S.,
801 2020. BayMBT: A Bayesian calibration model for branched glycerol dialkyl
802 glycerol tetraethers in soils and peats. Geochimica et Cosmochimica Acta
803 268, pp. 142-159.

804 Dang, X., Ding, W., Yang, H., Pancost, R.D., Naafs, B.D.A., Xue, J., Lin, X., Lu, J.
805 and Xie, S., 2018. Different temperature dependence of the bacterial
806 brGDGT isomers in 35 Chinese lake sediments compared to that in
807 soils. Organic Geochemistry 119, pp. 72-79.

808 Dee, S.G., Russell, J.M., Morrill, C., Chen, Z. and Neary, A., 2018. PRYSM v2. 0:
809 A proxy system model for lacustrine archives. Paleoceanography and
810 Paleoclimatology 33, pp. 1250-1269.

811 De Jonge, C., Stadnitskaia, A., Hopmans, E.C., Cherkashov, G., Fedotov, A. and
812 Damsté, J.S.S., 2014b. In situ produced branched glycerol dialkyl glycerol
813 tetraethers in suspended particulate matter from the Yenisei River, Eastern
814 Siberia. Geochimica et Cosmochimica Acta 125, pp. 476-491.

815 De Jonge, C., Hopmans, E.C., Zell, C.I., Kim, J.H., Schouten, S. and Damsté, J.S.S.,
816 2014a. Occurrence and abundance of 6-methyl branched glycerol dialkyl
817 glycerol tetraethers in soils: Implications for palaeoclimate
818 reconstruction. Geochimica et Cosmochimica Acta 141, pp. 97-112.

819 De Jonge, C., Hopmans, E.C., Stadnitskaia, A., Rijpstra, W.I.C., Hofland, R.,
820 Tegelaar, E. and Damsté, J.S.S., 2013. Identification of novel penta-and
821 hexamethylated branched glycerol dialkyl glycerol tetraethers in peat using

822 HPLC–MS2, GC–MS and GC–SMB-MS. Organic Geochemistry 54, pp. 78-
823 82.

824 Digerfeldt, G., 1986. Studies on Past Lake-Level Fluctuations. Handbook of
825 Holocene Palaeoecology and Palaeohydrology, pp. 127–143. John Wiley and
826 Sons, New York.

827 Dirghangi, S.S., Pagani, M., Hren, M.T. and Tipple, B.J., 2013. Distribution of
828 glycerol dialkyl glycerol tetraethers in soils from two environmental
829 transects in the USA. Organic Geochemistry 59, pp. 49-60.

830 Downing, J.A., Prairie, Y.T., Cole, J.J., Duarte, C.M., Tranvik, L.J., Striegl, R.G.,
831 McDowell, W.H., Kortelainen, P., Caraco, N.F., Melack, J.M. and
832 Middelburg, J.J., 2006. The global abundance and size distribution of lakes,
833 ponds, and impoundments. Limnology and Oceanography 51, pp. 2388-
834 2397.

835 Dyke, A.S., 2004. An outline of North American deglaciation with emphasis on
836 central and northern Canada. Developments in Quaternary Sciences 2, pp.
837 373-424.

838 Feng, X., Zhao, C., D'Andrea, W.J., Liang, J., Zhou, A. and Shen, J., 2019.
839 Temperature fluctuations during the Common Era in subtropical
840 southwestern China inferred from brGDGTs in a remote alpine lake. Earth
841 and Planetary Science Letters 510, pp. 26-36.

842 Fleming, L.E. and Tierney, J.E., 2016. An automated method for the determination
843 of the TEX86 and U37K′ paleotemperature indices. Organic Geochemistry
844 92, pp. 84-91.

Green, G.N. and Drouillard, P.H., 1994. The digital geologic map of Wyoming in ARC/INFO format. US Department of the Interior, US Geological Survey.

He, L., Zhang, C.L., Dong, H., Fang, B. and Wang, G., 2012. Distribution of glycerol dialkyl glycerol tetraethers in Tibetan hot springs. Geoscience Frontiers 3, pp. 289-300.

Hood, J.L., Roy, J.W. and Hayashi, M., 2006. Importance of groundwater in the water balance of an alpine headwater lake. Geophysical Research Letters 33, pp. 1-5.

Hopmans, E.C., Schouten, S. and Damsté, J.S.S., 2016. The effect of improved chromatography on GDGT-based palaeoproxies. Organic Geochemistry 93, pp. 1-6.

Hopmans, E.C., Weijers, J.W., Schefuß, E., Herfort, L., Damsté, J.S.S. and Schouten, S., 2004. A novel proxy for terrestrial organic matter in sediments based on branched and isoprenoid tetraether lipids. Earth and Planetary Science Letters 224, pp. 107-116.

Huguet, C., Hopmans, E.C., Febo-Ayala, W., Thompson, D.H., Damsté, J.S.S. and Schouten, S., 2006. An improved method to determine the absolute abundance of glycerol dibiphytanyl glycerol tetraether lipids. Organic Geochemistry 37, pp. 1036-1041.

Lee, L.Y.W., Chen, J.C. and Nelson, R.A., 1985. Liquid-solid contact measurements using a surface thermocouple temperature probe in atmospheric pool boiling water. International Journal of Heat and Mass Transfer 28, pp. 1415-1423.

867 Leng, M.J. and Marshall, J.D., 2004. Palaeoclimate interpretation of stable isotope
868 data from lake sediment archives. Quaternary Science Reviews 23, pp. 811-
869 831.

870 Liefert, D.T., Shuman, B.N., Parsekian, A.D. and Mercer, J.J., 2018. Why are some
871 rocky mountain lakes ephemeral? Water Resources Research 54, pp. 5245-
872 5263.

873 Loomis, S.E., Russell, J.M. and Lamb, H.F., 2015. Northeast African temperature
874 variability since the Late Pleistocene. Palaeogeography, Palaeoclimatology,
875 Palaeoecology 423, pp.80-90.

876 Loomis, S.E., Russell, J.M., Eggermont, H., Verschuren, D. and Damsté, J.S.S.,
877 2014b. Effects of temperature, pH and nutrient concentration on branched
878 GDGT distributions in East African lakes: Implications for
879 paleoenvironmental reconstruction. Organic Geochemistry 66, pp.25-37.

880 Loomis, S.E., Russell, J.M., Heureux, A.M., D'Andrea, W.J. and Damsté, J.S.S.,
881 2014a. Seasonal variability of branched glycerol dialkyl glycerol tetraethers
882 (brGDGTs) in a temperate lake system. Geochimica et Cosmochimica
883 Acta 144, pp. 173-187.

884 Loomis, S.E., Russell, J.M., Ladd, B., Street-Perrott, F.A. and Damsté, J.S.S., 2012.
885 Calibration and application of the branched GDGT temperature proxy on
886 East African lake sediments. Earth and Planetary Science Letters 357, pp.
887 277-288.

888 Marsicek, J., Shuman, B.N., Bartlein, P.J., Shafer, S.L. and Brewer, S., 2018.
889 Reconciling divergent trends and millennial variations in Holocene
890 temperatures. Nature 554, pp. 92-96.

891 Martínez-Sosa, P. and Tierney, J.E., 2019. Lacustrine brGDGT response to
892 microcosm and mesocosm incubations. Organic Geochemistry 127, pp. 12-
893 22.

894 MATLAB. 2019. version 9.6.0.1214997 (R2019a) Update 6. Natick, Massachusetts:
895 The MathWorks Inc.

896 Miller, D.R., Habicht, M.H., Keisling, B.A., Castañeda, I.S. and Bradley, R.S.,
897 2018. A 900-year New England temperature reconstruction from in situ
898 seasonally produced branched glycerol dialkyl glycerol tetraethers
899 (brGDGTs). Climate of the Past 14, pp. 1653–1667.

900 Minckley, T. A., Shriver, R. K., & Shuman, B. 2012. Resilience and regime change
901 in a southern Rocky Mountain ecosystem during the past 17 000
902 years. Ecological Monographs 82, pp. 49-68.

903 Musselman, R.C., 1994. The glacier lakes ecosystem experiments site. US
904 Department of Agriculture, Forest Service, Rocky Mountain Forest and
905 Range Experiment Station.

906 Naafs, B.D.A., Inglis, G.N., Zheng, Y., Amesbury, M.J., Biester, H., Bindler, R.,
907 Blewett, J., Burrows, M.A., Del Castillo Torres, D., Chambers, F.M. and
908 Cohen, A.D., 2017b. Introducing global peat-specific temperature and pH
909 calibrations based on brGDGT bacterial lipids. Geochimica et Cosmochimica
910 Acta 208, pp. 285-301.

911 Naafs, B.D.A., Gallego-Sala, A.V., Inglis, G.N. and Pancost, R.D., 2017a. Refining
912 the global branched glycerol dialkyl glycerol tetraether (brGDGT) soil
913 temperature calibration. Organic Geochemistry 106, pp. 48-56.

914 Ning, D., Zhang, E., Shulmeister, J., Chang, J., Sun, W. and Ni, Z., 2019. Holocene
915 mean annual air temperature (MAAT) reconstruction based on branched
916 glycerol dialkyl glycerol tetraethers from Lake Ximenglongtan, southwestern
917 China. Organic Geochemistry 133, pp. 65-76.

918 Parish, M.C., Calder, W.J. and Shuman, B.N., 2020. Millennial-scale increase in
919 winter precipitation in the southern Rocky Mountains during the Common
920 Era. Quaternary Research 94, pp. 1-13.

921 Parnell, A.C., Haslett, J., Allen, J.R., Buck, C.E. and Huntley, B., 2008. A flexible
922 approach to assessing synchroneity of past events using Bayesian
923 reconstructions of sedimentation history. Quaternary Science Reviews 27,
924 pp. 1872-1885.

925 Peterse, F., van der Meer, J., Schouten, S., Weijers, J.W., Fierer, N., Jackson, R.B.,
926 Kim, J.H. and Damsté, J.S.S., 2012. Revised calibration of the MBT–CBT
927 paleotemperature proxy based on branched tetraether membrane lipids in
928 surface soils. Geochimica et Cosmochimica Acta 96, pp. 215-229.

929 Peterse, F., Kim, J.H., Schouten, S., Kristensen, D.K., Koç, N. and Damsté, J.S.S.,
930 2009. Constraints on the application of the MBT/CBT palaeothermometer at
931 high latitude environments (Svalbard, Norway). Organic Geochemistry 40,
932 pp. 692-699.

933 Polanco-Martinez, J.M., Medina-Elizalde, M.A., Goni, M.F.S. and Mudelsee, M.,
934 2019. BINCOR: An R package for Estimating the Correlation between Two
935 Unevenly Spaced Time Series. The R Journal 11, pp. 1-14.

936 Pribyl, P. and Shuman, B.N., 2014. A computational approach to Quaternary lake-
937 level reconstruction applied in the central Rocky Mountains, Wyoming,
938 USA. Quaternary Research 82, pp. 249-259.

939 PRISM Climate Group, Oregon State University, http://prism.oregonstate.edu,
940 created June 2018.

941 R Core Team, 2018. R: A language and environment for statistical computing. R
942 Foundation for Statistical Computing, Vienna, Austria. URL https://www.R-
943 project.org/.

944 Rautio, A. and Korkka-Niemi, K., 2011. Characterization of groundwater–lake water
945 interactions at Pyhäjärvi, a lake in SW Finland. Boreal Environment
946 Research 16: pp. 363–380.

947 Rosenberry, D. O., & LaBaugh, J. W., 2008. Field techniques for estimating water
948 fluxes between surface water and ground. USGS, Reston, Virginia.

949 Russell, J.M., Hopmans, E.C., Loomis, S.E., Liang, J. and Damsté, J.S.S., 2018.
950 Distributions of 5-and 6-methyl branched glycerol dialkyl glycerol
951 tetraethers (brGDGTs) in East African lake sediment: Effects of temperature,
952 pH, and new lacustrine paleotemperature calibrations. Organic
953 Geochemistry 117, pp. 56-69.

954 Rust, R.A. and Minckley, T.A., 2020. Fire and hydrologically mediated diversity
955 change in subalpine forests through the Holocene. Journal of Vegetation
956 Science 31, pp. 380-391.

957 Schoon, P.L., de Kluijver, A., Middelburg, J.J., Downing, J.A., Damsté, J.S.S. and
958 Schouten, S., 2013. Influence of lake water pH and alkalinity on the
959 distribution of core and intact polar branched glycerol dialkyl glycerol
960 tetraethers (GDGTs) in lakes. Organic Geochemistry 60, pp. 72-82.

961 Schouten, S., Hopmans, E.C., Pancost, R.D. and Damsté, J.S.S., 2000. Widespread
962 occurrence of structurally diverse tetraether membrane lipids: evidence for
963 the ubiquitous presence of low-temperature relatives of
964 hyperthermophiles. Proceedings of the National Academy of Sciences 97,
965 pp. 14421-14426.

966 Sinninghe Damsté, J.S., 2016. Spatial heterogeneity of sources of branched
967 tetraethers in shelf systems: The geochemistry of tetraethers in the Berau
968 River delta (Kalimantan, Indonesia). Geochimica et Cosmochimica Acta
969 186, pp. 13-31.

970 Sinninghe Damsté, J.S., Ossebaar, J., Abbas, B., Schouten, S. and Verschuren, D.,
971 2009. Fluxes and distribution of tetraether lipids in an equatorial African
972 lake: constraints on the application of the TEX86 palaeothermometer and
973 BIT index in lacustrine settings. Geochimica et Cosmochimica Acta 73, pp.
974 4232-4249.

975 Sinninghe Damsté, J.S., Hopmans, E.C., Pancost, R.D., Schouten, S. and
976 Geenevasen, J.A., 2000. Newly discovered non-isoprenoid glycerol dialkyl

977 glycerol tetraether lipids in sediments. Chemical Communications 17, pp.
978 1683-1684.

979 Shuman, B.N. and Serravezza, M., 2017. Patterns of hydroclimatic change in the
980 Rocky Mountains and surrounding regions since the last glacial
981 maximum. Quaternary Science Reviews 173, pp. 58-77.

982 Shuman, B.N. and Marsicek, J., 2016. The structure of Holocene climate change in
983 mid-latitude North America. Quaternary Science Reviews 141, pp. 38-51.

984 Shuman, B., 2012. Recent Wyoming temperature trends, their drivers, and impacts
985 in a 14,000-year context. Climatic Change 112, pp. 429-447.

986 Tierney, J.E., Malevich, S.B., Gray, W., Vetter, L. and Thirumalai, K., 2019.
987 Bayesian calibration of the Mg/Ca paleothermometer in planktic
988 foraminifera. Paleoceanography and Paleoclimatology 34, pp. 2005-2030.

989 Tierney, J.E. and Tingley, M.P., 2014. A Bayesian, spatially-varying calibration
990 model for the TEX86 proxy. Geochimica et Cosmochimica Acta 127, pp. 83-
991 106.

992 Tierney, J.E., Schouten, S., Pitcher, A., Hopmans, E.C. and Damsté, J.S.S., 2012.
993 Core and intact polar glycerol dialkyl glycerol tetraethers (GDGTs) in Sand
994 Pond, Warwick, Rhode Island (USA): Insights into the origin of lacustrine
995 GDGTs. Geochimica et Cosmochimica Acta 77, pp. 561-581.

996 Tierney, J.E., Russell, J.M., Eggermont, H., Hopmans, E.C., Verschuren, D. and
997 Damsté, J.S., 2010. Environmental controls on branched tetraether lipid

998 distributions in tropical East African lake sediments. Geochimica et
999 Cosmochimica Acta 74, pp. 4902-4918.

1000 Tierney, J.E. and Russell, J.M., 2009. Distributions of branched GDGTs in a tropical
1001 lake system: implications for lacustrine application of the MBT/CBT
1002 paleoproxy. Organic Geochemistry 40, pp. 1032-1036.

1003 Weber, Y., Damsté, J.S.S., Zopfi, J., De Jonge, C., Gilli, A., Schubert, C.J., Lepori,
1004 F., Lehmann, M.F. and Niemann, H., 2018. Redox-dependent niche
1005 differentiation provides evidence for multiple bacterial sources of glycerol
1006 tetraether lipids in lakes. Proceedings of the National Academy of
1007 Sciences 115, pp. 10926-10931.

1008 Weijers, J.W., Panoto, E., van Bleijswijk, J., Schouten, S., Rijpstra, W.I.C., Balk,
1009 M., Stams, A.J. and Damste, J.S.S., 2009. Constraints on the biological
1010 source (s) of the orphan branched tetraether membrane
1011 lipids. Geomicrobiology Journal 26, pp. 402-414.

1012 Weijers, J.W., Schouten, S., van den Donker, J.C., Hopmans, E.C. and Damsté,
1013 J.S.S., 2007. Environmental controls on bacterial tetraether membrane lipid
1014 distribution in soils. Geochimica et Cosmochimica Acta 71, pp. 703-713.

1015 Weijers, J.W., Schouten, S., Hopmans, E.C., Geenevasen, J.A., David, O.R.,
1016 Coleman, J.M., Pancost, R.D. and Sinninghe Damsté, J.S., 2006. Membrane
1017 lipids of mesophilic anaerobic bacteria thriving in peats have typical archaeal
1018 traits. Environmental Microbiology 8, pp. 648-657.

1019 Whitlock, C. and Bartlein, P.J., 1993. Spatial variations of Holocene climatic change
1020 in the Yellowstone region. Quaternary Research 39, pp. 231-238.

1021 Winter, T.C., 1976. Numerical simulation analysis of the interaction of lakes and
1022 ground water. US Geological Survey Professional Paper 1001.

1023 Wurzbacher, C., Fuchs, A., Attermeyer, K., Frindte, K., Grossart, H.P., Hupfer, M.,
1024 Casper, P. and Monaghan, M.T., 2017. Shifts among Eukaryota, Bacteria,
1025 and Archaea define the vertical organization of a lake
1026 sediment. Microbiome 5, pp. 1-16.

1027 Zell, C., Kim, J.H., Moreira-Turcq, P., Abril, G., Hopmans, E.C., Bonnet, M.P.,
1028 Sobrinho, R.L. and Damsté, J.S.S., 2013. Disentangling the origins of
1029 branched tetraether lipids and crenarchaeol in the lower Amazon River:
1030 Implications for GDGT-based proxies. Limnology and Oceanography 58, pp.
1031 343-353.

1032 Zhu, C., Weijers, J.W., Wagner, T., Pan, J.M., Chen, J.F. and Pancost, R.D., 2011.
1033 Sources and distributions of tetraether lipids in surface sediments across a
1034 large river-dominated continental margin. Organic Geochemistry 42, pp.
1035 376-386.

1036 Figure captions:

1037 Fig. 1. Map showing the location of 34 lakes sampled (circles and diamond) with
1038 elevation as color scale. The diamond symbol represents the location of
1039 Lower Paintrock Lake where we applied our brGDGT calibration.

1040 Fig. 2. Boxplot showing the fractional abundances of individual brGDGTs in lake
1041 surface sediment samples from: A) all lakes - all sampling depths, n=39; B)
1042 shallow lakes (this study: sample depth <3 meters, n=17); C) deep lakes (this
1043 study: sample depth >3 meters, n=22). Box plot interpretation: lower whisker
1044 shows the lowest value, lower hinge shows the first quantile (the 25^{th}
1045 percentile), middle hinge shows second quantile (50^{th} percentile or the
1046 median,) upper hinge shows the third quantile (75^{th} percentile) and the upper
1047 whisker shows the highest value.

1048 Fig. 3. Sediment sampling depth in meters versus MBT'_{5Me} with elevation for color
1049 scale, (n=39).

1050 Fig. 4. Grouped fractional abundances of tetra-, penta- and hexa-methylated
1051 brGDGTs (n=17) versus: A) Mean summer air temperature (JJAS); B)
1052 Summer lake surface temperature (T_{SURF}); C) Summer lake bottom
1053 temperature (T_{BOT}). Spearman's correlation coefficients (r) and associated p-
1054 values are shown in each subplot.

1055 Fig. 5. MBT'_{5Me} values as a function of modern sediment depth at Round (open
1056 triangles), Rainbow Lake (filled circles) and Duncan Lake (filled squares)
1057 located at elevations of 3232m, 3000, and 2800 m, respectively.

Fig. 6. Relationship between the MBT'$_{5Me}$ index and: A) Mean summer air temperature (JJAS), n=39; B) Summer lake surface temperatures (T_{SURF}), n=17; C) Summer lake bottom temperatures (T_{BOT}), n=17. Diamonds represent shallow lakes (<3m) and circles represent deep lakes (>3m). Regression lines represent the relationship between the individual variables (JJAS, T_{SURF} and T_{BOT}) and the MBT'$_{5Me}$ index for: shallow lakes (red dashed line), deep lakes (blue dashed line) and all depths (black solid line).

Fig. 7. Observed T_{BOT} versus Bayesian estimated T_{BOT}. Solid line denotes the 1:1 reference line and residuals are plotted atop.

Fig. 8. A) Observed MBT'$_{5Me}$ index versus Bayesian estimated MBT'$_{5Me}$ index; B) Observed mean summer air temperatures (JJAS) versus Bayesian estimated JJAS temperatures; C) Observed ln(water depth) versus Bayesian estimated ln(water depth). Solid lines denote the 1:1 reference lines and residuals are plotted atop each scatterplot. LPR is shown in red.

Fig. 9. A) Laurentide Ice Sheet percent area (light blue shaded area) [Dyke A. 2004] and the insolation curve at 60°N (red line) [Berger and Loutre, 1991]. B) Reconstructed T_{BOT} (diamonds) at Lower Paintrock Lake, shaded grey area represents the central 50% credible interval. C) BrGDGT-based JJAS (black line) at Lower Paintrock Lake, shaded grey area represents the central 50% credible interval; pollen-based JJAS (orange line), shaded light orange area represents ±RMSE (RMSE=1.8 °C). D) The water depth history (blue dashed line) at Lower Paintrock Lake, WY. All versus calibrated kyrs before 1950.

Table 1. Site locations and environmental data

Lake	Latitude	Longitude	Elevation (m)	Maximum depth (m)	Sample water depth (m)	Summer water temperature °C		MAAT °C	JJAS °C	MBT'_{5Me}	MAAT °C Russell et al. 2018	MAAT °C Dang et al. 2018
						top	bottom					
Bear	40.775°N	106.631°W	3182	6	6			0.6	10.2	0.152	3.7	-5.6
Beaver	40.754°N	106.686°W	3176	5.5	5.5			0.6	10.1	0.213	5.7	-0.7
Brooklyn	41.373°N	106.249°W	3233	11.6	11.6	13.8	6.7	-0.2	8.9	0.199	5.3	-2.2
Crater	41.491°N	106.247°W	3001	19.8	16	15.2	4.3	0.9	10.2	0.176	4.5	-1.9
Duncan	44.647°N	107.447°W	2798	1.8	1.8			0.8	10	0.368	10.7	7
East Glacier	41.377°N	106.259°W	3312	7.6	6	13.4	12	-0.4	8.5	0.129	2.9	-6.4
Eileen	40.903°N	106.673°W	3168	5.7	5.7			0	9.5	0.235	6.4	0.1
Fire Box	41.442°N	106.193°W	2935	1	0.5	20.6	20.1	1.6	10.7	0.4	11.8	10.3
Fishhook	41.357°N	106.267°W	3232	1.7	1.7	13.6	13.6	0	9	0.288	8.1	6.5
Gem	40.881°N	106.734°W	3180	6.5	6.5			0.2	9.4	0.221	5.9	0.4
Highway 130	41.351°N	106.264°W	3201	1.5	0.8	14.6	14.5	0.2	9.2	0.332	9.6	9.9
Hourglass	41.350°N	106.271°W	3214	1.2	1.1	13.1	12.9	0.2	9.1	0.353	10.2	6.5
Lewis	41.359°N	106.296°W	3311	10.1	9.9	15.2	8.4	-0.6	8.5	0.201	5.4	0.4
Libby Flats	41.324°N	106.286°W	3199	1.2	0.5			0.2	9.2	0.397	11.6	13.4
Libby Flats 1	41.332°N	106.294°W	3233	0.89	0.89			0..1	9	0.341	9.9	7.1
Libby Flats 3	41.319°N	106.280°W	3200	0.49	0.49			0.1	9.1	0.38	11.1	12.5
Libby	41.354°N	106.298°W	3297	12.2	10.3	12.5	7.7	-0.6	8.5	0.159	3.9	-2.4
Little Jeep	41.353°N	106.277°W	3252	1.5	1.5			0.2	8.9	0.339	9.8	6.2
Lost	41.445°N	106.118°W	2819	1	0.6	16.2	16.1	2.2	11.3	0.342	9.9	8.6
Lower Paintrock	44.390°N	107.380°W	2814	5.8	5.8			0.6	10	0.239	6.5	3.3
Middle Rainbow	40.648°N	106.624°W	3016	5.8	5.8			1.2	10.6	0.227	6.2	2.4
Mirror Lake	41.338°N	106.320°W	3241	15.7	15.7	12.9	5.8	-0.3	8.9	0.205	5.4	-4.8
North Banner	41.415°N	106.358°W	3040	4.2	3.3	19.2	16.6	1.1	10.1	0.267	7.4	0.4
Rainbow	44.936°N	109.500°W	2959	2.5	1			0.8	8.2	0.314	9	2.9
Round	41.359°N	106.269°W	3249	1.2	1.2	15.9	13.6	0	8.9	0.256	7.1	6.1
Round Mountain	40.585°N	106.678°W	3045	3.5	3.5			1.3	10.6	0.241	6.6	0.9
Seven	40.896°N	106.681°W	3250	5.8	5.8			0	9.4	0.234	6.4	-0.8
Silver	41.309°N	106.357°W	3191	7.6	7	14.3	8.9	-0.1	9	0.179	4.6	1.4
Silver Run	41.327°N	106.237°W	3068	4.3	4.3	15.8	13.2	0.9	9.9	0.266	7.4	6.7
South Gap	41.369°N	106.299°W	3369	21.3	16.2	12.2	5.6	-0.8	8.2	0.099	2	-7.3
Stamp Mill	41.350°N	106.381°W	3039	3.9	3.9	18.6	16.2	1.1	10	0.291	8.2	3
Teal	40.583°N	106.608°W	2700	13.1	13.1			2.6	12	0.314	9	7.1
Unnamed	40.506°N	106.617°W	2797	6	6			2.1	11.7	0.29	8.2	5.1
Whale	40.556°N	106.675°W	3086	11.5	11.5			1.1	10.6	0.215	5.8	-0.2

Table 2. Pairwise correlations of environmental data. Statistically significant correlations are shown in bold.

Spearman's correlations	Elevation m	Water depth m	MAAT °C	JJAS °C	T_{SURF} °C	T_{BOT} °C	Average water temp. °C	DO_{SURF} mg/L	DO_{BOT} mg/L	pH_{SURF}
Water depth m	r=0.25 p=0.125 n=39	-	-	-	-	-	-	-	-	-
MAAT °C	**r=-0.84** **p<0.001** **n=-39**	r=-0.19 p=0.252 n=39	-	-	-	-	-	-	-	-
JJAS °C	**r=-0.62** **p<0.001** **n=39**	r=0.02 p=0.912 n=39	**r=0.75** **p<0.001** **n=39**	-	-	-	-	-	-	-
T_{SURF} °C	**r=-0.78** **p<0.001** **n=17**	**r=-0.56** **p=0.018** **n=17**	**r=0.80** **p<0.001** **n=17**	**r=0.73** **p<0.001** **n=17**	-	-	-	-	-	-
T_{BOT} °C	**r=-0.64** **p=0.005** **n=17**	**r=-0.89** **p<0.001** **n=17**	**r=0.73** **p<0.001** **n=17**	**r=0.60** **p=0.011** **n=17**	**r=0.73** **p<0.001** **n=17**	-	-	-	-	-
Average water temp. °C	**r=-0.68** **p=0.003** **n=17**	**r=-0.67** **p=0.003** **n=17**	**r=0.69** **p=0.002** **n=17**	**r=0.64** **p=0.005** **n=17**	**r=0.64** **p=0.006** **n=17**	**r=0.83** **p<0.001** **n=17**	-	-	-	-
DO_{SURF} mg/L	r=0.05 p=0.864 n=16	r=-0.13 p=0.629 n=16	r=0.03 p=0.918 n=16	r=0.02 p=0.957 n=16	r=0.19 p=0.479 n=16	r=0.16 p=0.557 n=16	r=0.10 p=0.712 n=16	-	-	-
DO_{BOT} mg/L	r=-0.36 p=0.166 n=16	**r=-0.66** **p=0.005** **n=16**	r=0.47 p=0.070 n=16	r=0.39 p=0.140 n=16	**r=0.54** **p=0.032** **n=16**	**r=0.71** **p=0.002** **n=16**	**r=0.75** **p<0.001** **n=16**	r=0.45 p=0.081 n=16	-	-
pH_{SURF}	r=-0.36 p=0.197 n=16	r=-0.27 p=0.337 n=16	r=-0.20 p=0.274 n=16	r=-0.26 p=0.351 n=16	r=-0.33 p=0.223 n=16	r=-0.33 p=0.223 n=16	r=-24 p=0.394 n=16	r=0.51 p=0.055 n=16	r=0.11 p=0.708 n=16	-
pH_{BOT}	**r=-0.52** **p=0.045** **n=16**	**r=-0.67** **p=0.006** **n=16**	**r=0.60** **p=0.018** **n=16**	**r=0.62** **p=0.014** **n=16**	r=0.43 p=0.113 n=16	**r=0.56** **p=0.031** **n=16**	**r=0.59** **p=0.022** **n=16**	r=0.34 p=0.215 n=16	**r=0.68** **p=0.005** **n=16**	r=0.34 p=0.208 n=16

Table 3. Pairwise correlations between environmental variables and the MBT'$_{5Me}$ and CBT' indices. Statistically significant correlations are shown in bold.

Spearman's correlations	MBT'$_{5Me}$	CBT'
MAAT °C	**r=0.436** **p=0.006** **n=39**	r=-0.128 p=0.438 n=39
JJAS °C	r=0.208 p=0.203 n=39	r=-0.178 p=0.278 n=39
T_{BOT} °C	**r=0.790** **p<0.001** **n=17**	r=-0.159 p=0.0.541 n=17
T_{TOP} °C	**r=0.565** **p=0.018** **n=17**	r=-0.221 p=0.392 n=17
DO_{BOT} mg/L	**r=0.632** **p=0.009** n=16	r=-0.035 p=0.897 n=16
DO_{TOP} mg/L	r=0.152 p=0.575 n=16	r=-0.262 p=0.327 n=16
pH_{BOT}	**r=0.606** **p=0.017** **n=16**	r=0.298 p=0.280 n=16
pH_{TOP}	r=-0.198 p=0.478 n=16	r=0.295 p=0.286 n=16

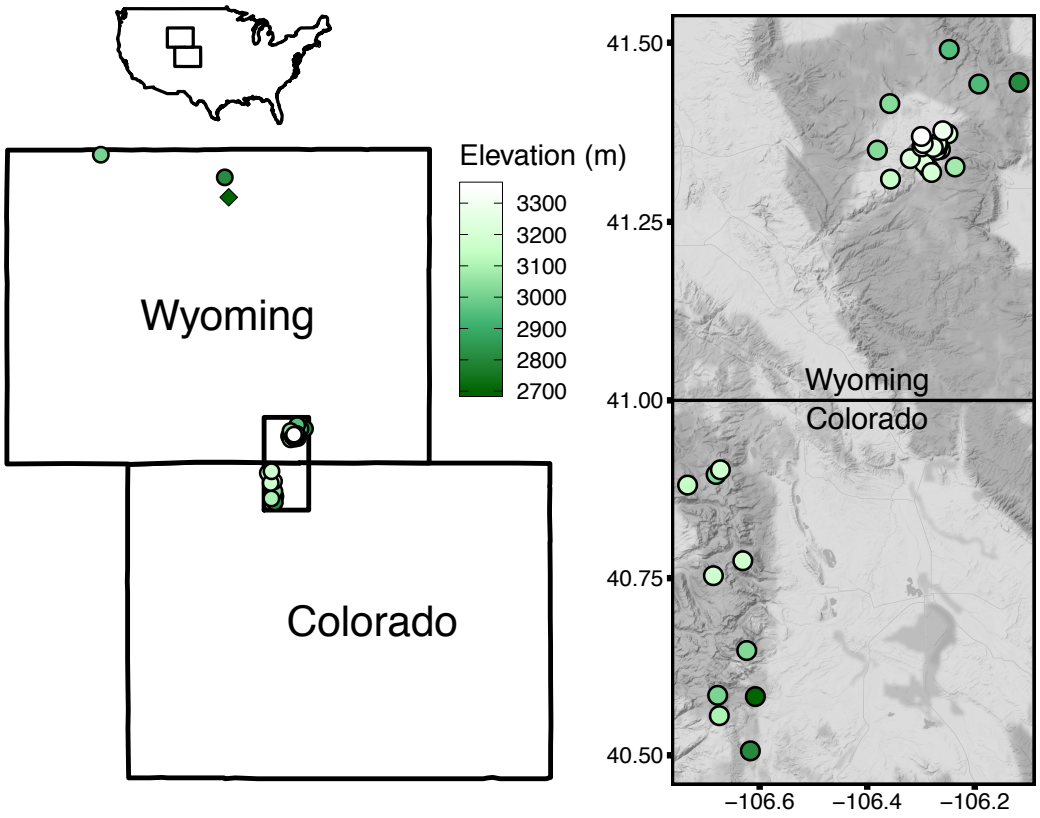
Wyoming
Colorado
Elevation (m)
3300
3200
3100
3000
2900
2800
2700
41.50
41.25
41.00
40.75
40.50
−106.6
−106.4
−106.2
Wyoming
Colorado

Figure 1.

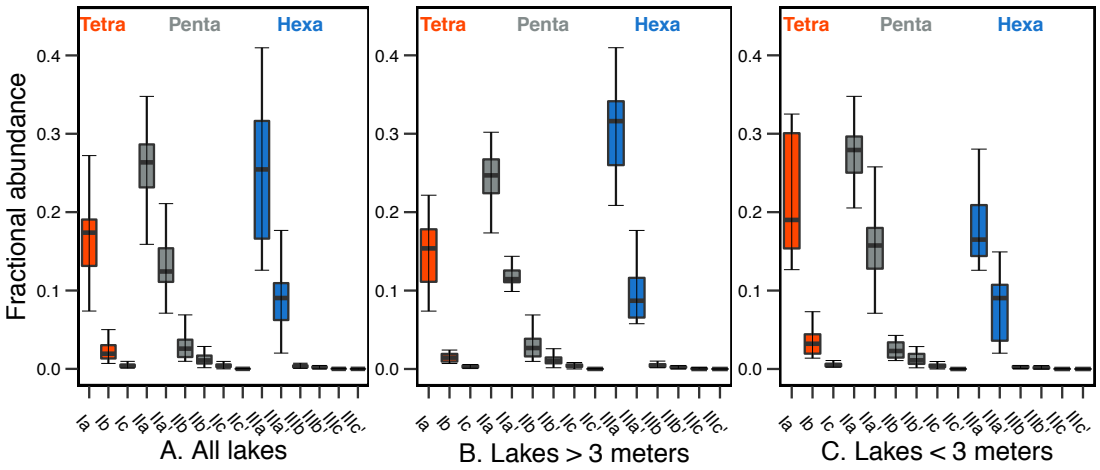
Tetra
Penta
Hexa
Fractional abundance
0.0
0.1
0.2
0.3
0.4
Ia
Ib
Ic
IIa
IIa,b
IIb
IIc
IIc,
IIIa
IIIa,b
IIIb
IIIc
IIIc,
A. All lakes
B. Lakes > 3 meters
C. Lakes < 3 meters

Figure 2.

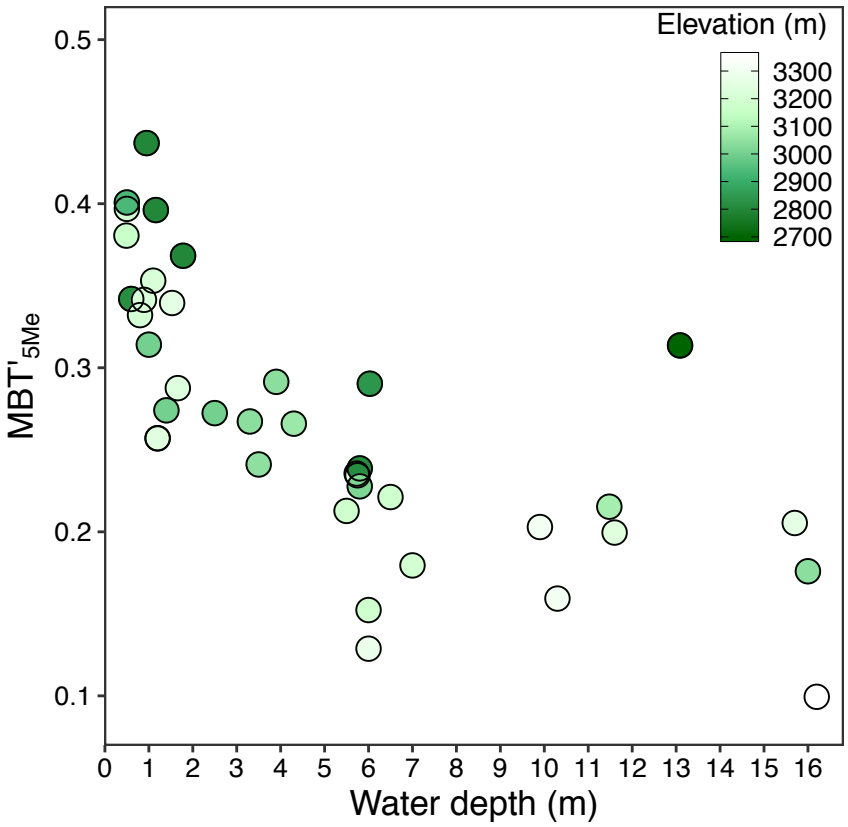
Elevation (m)
3300
3200
3100
3000
2900
2800
2700
MBT'5Me
0.5
0.4
0.3
0.2
0.1
0 1 2 3 4 5 6 7 8 9 10 11 12 13 14 15 16
Water depth (m)

Figure 3.

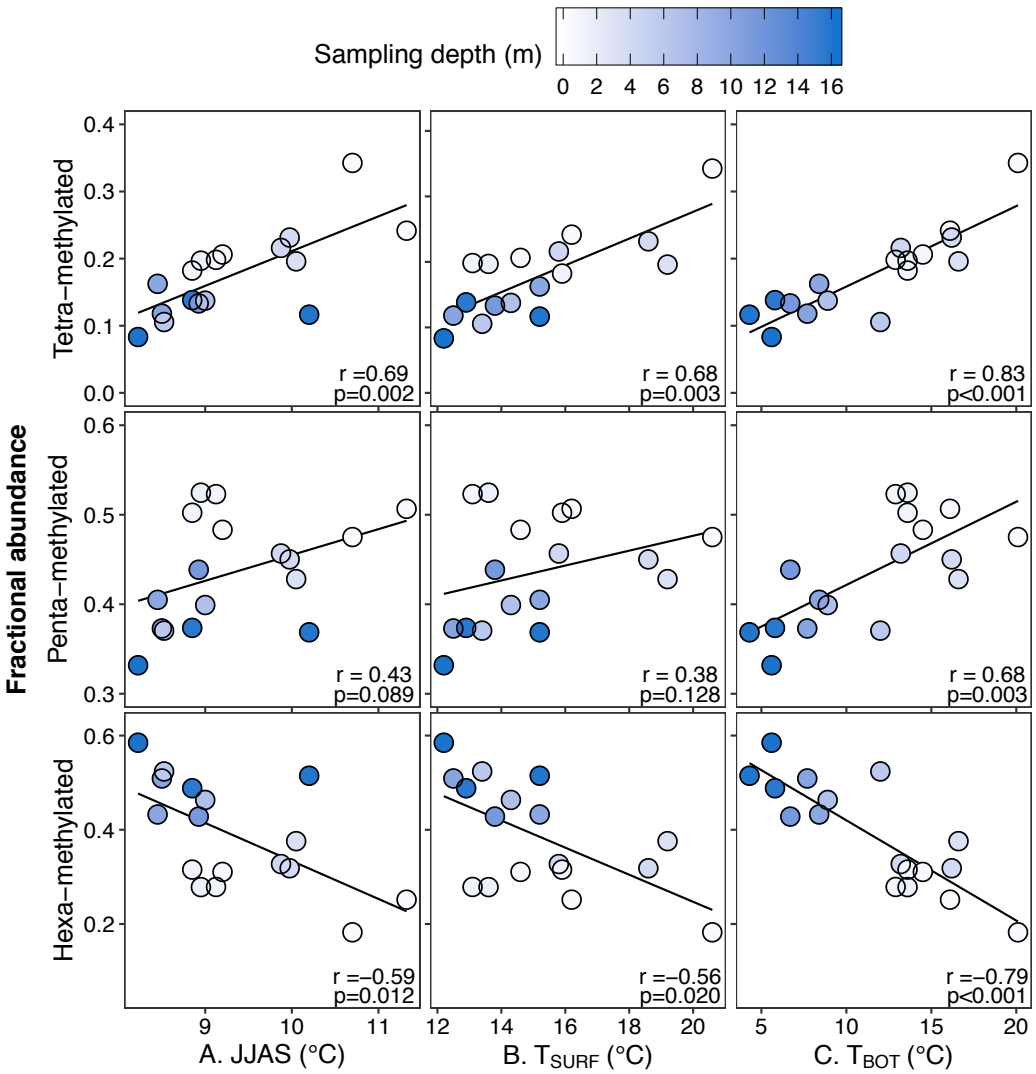
Sampling depth (m)
0 2 4 6 8 10 12 14 16
Fractional abundance
Tetra−methylated
Penta−methylated
Hexa−methylated
r =0.69
p=0.002
r = 0.68
p=0.003
r = 0.83
p<0.001
r = 0.43
p=0.089
r = 0.38
p=0.128
r = 0.68
p=0.003
r =−0.59
p=0.012
r =−0.56
p=0.020
r =−0.79
p<0.001
A. JJAS (°C)
B. T$_{SURF}$ (°C)
C. T$_{BOT}$ (°C)

Figure 4.

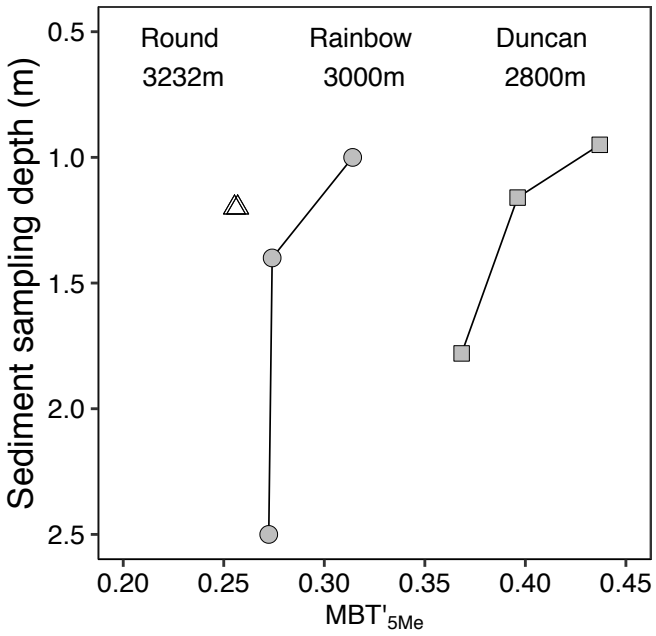
Round
3232m
Rainbow
3000m
Duncan
2800m
Sediment sampling depth (m)
0.5
1.0
1.5
2.0
2.5
0.20
0.25
0.30
0.35
0.40
0.45
MBT'5Me

Figure 5.

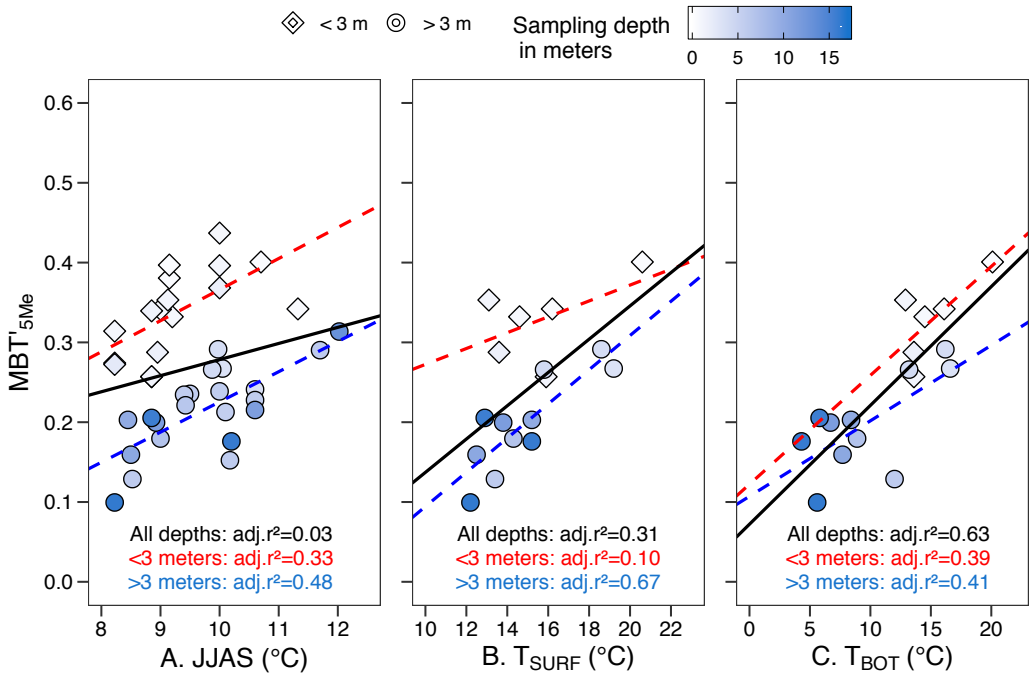
< 3 m
> 3 m
Sampling depth in meters
0
5
10
15
MBT'5Me
0.0
0.1
0.2
0.3
0.4
0.5
0.6
All depths: adj.r²=0.03
<3 meters: adj.r²=0.33
>3 meters: adj.r²=0.48
8
9
10
11
12
A. JJAS (°C)
All depths: adj.r²=0.31
<3 meters: adj.r²=0.10
>3 meters: adj.r²=0.67
10
12
14
16
18
20
22
B. TSURF (°C)
All depths: adj.r²=0.63
<3 meters: adj.r²=0.39
>3 meters: adj.r²=0.41
0
5
10
15
20
C. TBOT (°C)

Figure 6.

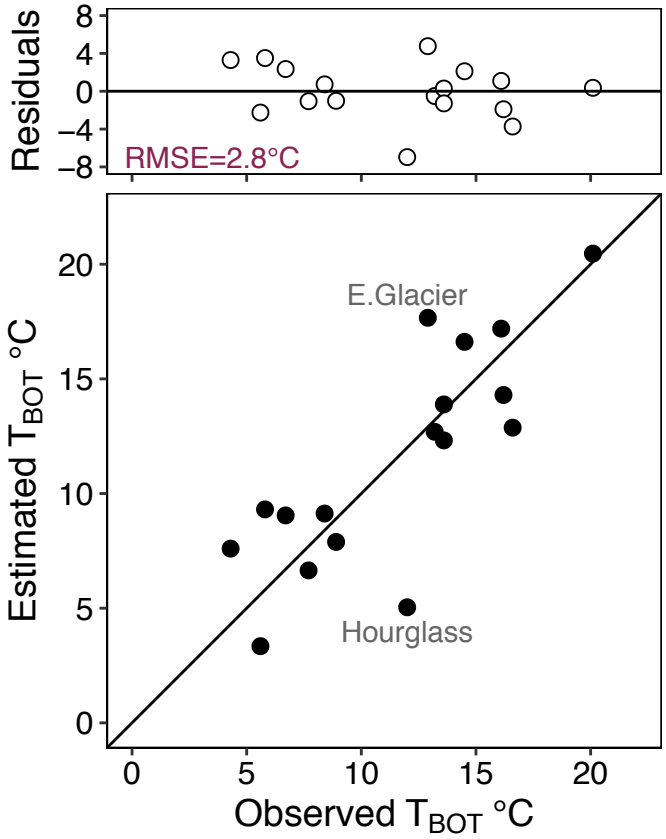
Residuals
8
4
0
−4
−8
RMSE=2.8°C
Estimated T_{BOT} °C
20
15
10
5
0
E.Glacier
Hourglass
0
5
10
15
20
Observed T_{BOT} °C

Figure 7.

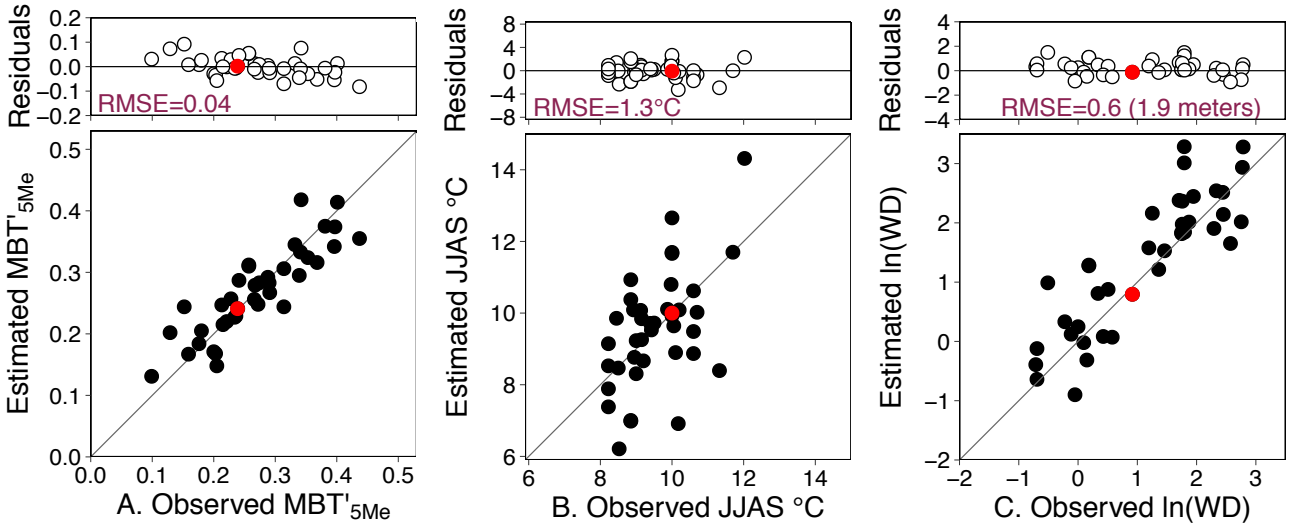
Residuals
RMSE=0.04
Estimated MBT'5Me
A. Observed MBT'5Me
Residuals
RMSE=1.3°C
Estimated JJAS °C
B. Observed JJAS °C
Residuals
RMSE=0.6 (1.9 meters)
Estimated ln(WD)
C. Observed ln(WD)

Figure 8.

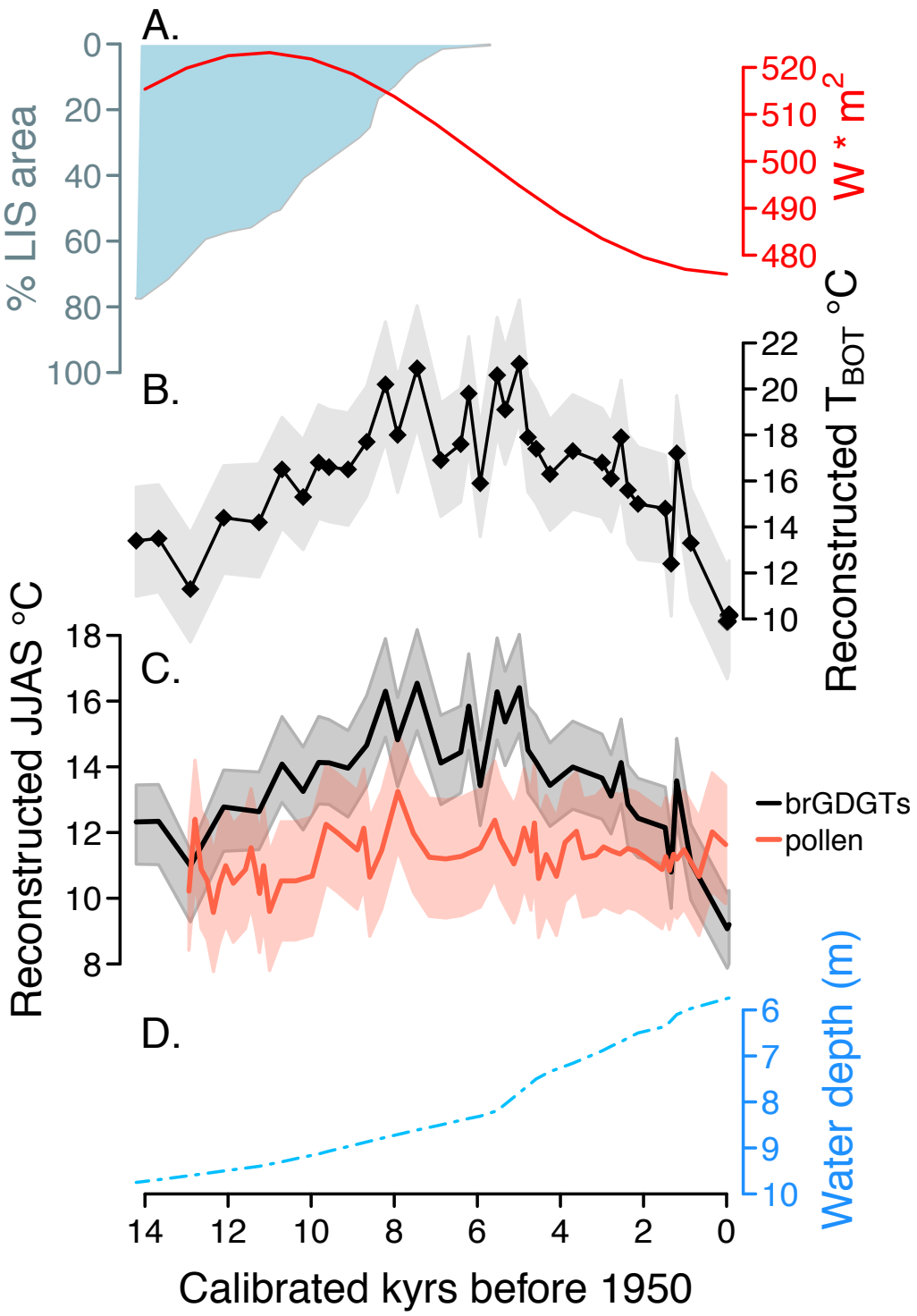
A.
% LIS area
0
20
40
60
80
100
520
510
500
490
480
W * m2
B.
Reconstructed TBOT °C
22
20
18
16
14
12
10
C.
Reconstructed JJAS °C
18
16
14
12
10
8
brGDGTs
pollen
D.
Water depth (m)
6
7
8
9
10
14
12
10
8
6
4
2
0
Calibrated kyrs before 1950

Figure 9.

Supplementary material

Supplementary Table 1. Dissolved oxygen concentrations and pH

Lake	Latitude	Longitude	Elevation (m)	Maximum depth (m)	Sample water depth (m)	Dissolved oxygen mg/L		pH	
						top	bottom	top	bottom
Brooklyn	41.373°N	106.249°W	3233	11.6	11.6	7.37	8.36	8.4	7.0
Crater	41.491°N	106.247°W	3001	19.8	16	7.45	0.01	8.2	7.0
East Glacier	41.377°N	106.259°W	3312	7.6	6	7.21	5.21	7.7	6.9
Fire Box	41.442°N	106.193°W	2935	1	0.5	8.87	8.87	6.8	7.7
Highway 130	41.351°N	106.264°W	3201	1.5	0.8	7.7	7.7	8.7	8.7
Hourglass	41.350°N	106.271°W	3214	1.2	1.1	7.45	7.45	8.9	8.9
Lewis	41.359°N	106.296°W	3311	10.1	9.9	7.54	3.73	7.9	6.3
Libby	41.354°N	106.298°W	3297	12.2	10.3	7.38	0.93	7.8	6.4
Lost	41.445°N	106.118°W	2819	1	0.6	5.6	6.69	7.4	7.0
Mirror Lake	41.338°N	106.320°W	3241	15.7	15.7	7.3	0.47	7.7	6.3
North Banner	41.415°N	106.358°W	3040	4.2	3.3	8.03	12.1	7.9	8.0
Round	41.359°N	106.269°W	3249	1.2	1.2	7.57	7.57		
Silver	41.309°N	106.357°W	3191	7.6	7	7.36	0.17	7.9	6.5
Silver Run	41.327°N	106.237°W	3068	4.3	4.3	8.23	7.61	9.6	9.7
South Gap	41.369°N	106.299°W	3369	21.3	16.2	8.06	3.23	8.7	6.0
Stamp Mill	41.350°N	106.381°W	3039	3.9	3.9	6.15	6.15	6.9	6.4

Supplementary Table 2. Radiocarbon analyses

Core	Depth (m)	Thickness (cm)	Lab No.	Material	^{14}C yr B.P.	Error (yr)	Calibrated age range B.P.		
							5%	Median	95%
LCA	29.5	1	UCIAMS-OS-95575	Bulk	1200	25	1080	1123	1171
LCA	69.5	1	UCIAMS-OS-95576	Bulk	1670	25	1537	1571	1603
LCA	70.5	2	UCIAMS-106149	Charcoal 0.17 mg C	1305	15	1187	1262	1283
LCA	134.5	2	UCIAMS-106150	Charcoal 0.16 mg C	3240	15	3443	3455	3473
LCA	167.5	1	UCIAMS-OS-95573	Bulk	4030	30	4439	4485	4527
LCA	189.5	1	UCIAMS-OS-95574	Bulk	4160	30	4628	4705	4821
LCA	252.5	2	UCIAMS-106151	Charcoal 0.067 mg C	4905	40	5598	5635	5655
LCA	371.5	1	UCIAMS-OS-95572	Bulk	10150	40	11729	11829	11968
LCA	372.5	2	UCIAMS-106152	Charcoal 0.14 mg C	10100	25	11620	11711	11767
LCA	393.5	1	UCIAMS-OS-95577	Bulk	11650	45	13409	13496	13580
LCA	402.5	1	UCIAMS-OS-95598	Bulk	11350	50	13168	13229	13286
LCA	461.5	1	UCIAMS-OS-95603	Bulk	17050	130	20069	20244	20423

Supplementary Table 3. Downcore ages, MBT'$_{5Me}$ values, mean summer air temperature (JJAS) and summer lake bottom temperature reconstructions at Lower Paintrock Lake, WY.

	Calibrated age range B.P.				Estimated JJAS°C			Estimated temperature bottom °C		
Depth (cm)	Median	5%	95%	MBT'$_{5Me}$	Median	25%	75%	Median	25%	75%
0.5	-59	-68	9	0.219	9.2	8.1	10.3	10.2	7.8	12.5
1.5	-16	-50	343	0.215	9.1	8.0	10.1	9.9	7.4	12.3
23.5	862	294	1070	0.274	11.1	10.0	12.2	13.3	7.1	19.5
36.5	1200	1098	1406	0.344	13.6	12.5	14.8	17.2	11.2	23.8
49.5	1334	1143	1513	0.261	10.8	9.7	11.9	12.4	6.3	18.5
62.5	1477	1185	1576	0.300	12.1	11.1	13.4	14.8	8.7	21.0
76.5	2132	1720	2824	0.306	12.4	11.3	13.7	15.0	9.1	21.5
87.5	2375	1871	3103	0.316	12.8	11.7	14.1	15.6	9.7	22.1
95.5	2540	1980	3201	0.354	14.1	13.0	15.5	17.9	11.8	24.4
105.5	2782	2133	3293	0.323	13.1	12.0	14.3	16.1	10.0	22.4
115.5	2997	2331	3361	0.337	13.7	12.5	15.0	16.8	10.8	23.3
142.5	3703	3505	4202	0.345	14.0	12.9	15.4	17.3	11.1	23.9
160.5	4252	3769	4436	0.327	13.4	12.3	14.7	16.3	10.1	22.7
176.5	4584	4488	4719	0.347	14.1	12.9	15.6	17.4	11.4	24.0
191.5	4782	4647	5029	0.356	14.5	13.4	15.9	17.9	12.1	24.5
206.5	4988	4743	5406	0.410	16.4	15.0	18.1	21.1	14.9	28.1
231.5	5331	4929	5585	0.378	15.4	14.1	16.9	19.1	13.0	25.7
245.5	5522	5130	5650	0.403	16.3	15.0	17.9	20.6	14.1	27.6
257.5	5930	5672	7381	0.320	13.4	12.3	14.7	15.9	9.9	22.3
262.5	6207	5732	7964	0.389	15.8	14.5	17.4	19.8	13.7	26.3
266.5	6400	5780	8288	0.348	14.4	13.3	15.8	17.6	11.5	24.3
276.5	6879	5901	9122	0.338	14.1	12.9	15.6	16.9	10.9	23.5
287.5	7449	6044	9627	0.407	16.5	15.2	18.1	20.9	14.5	27.9
297.5	7919	6199	10132	0.356	14.8	13.6	16.3	18.0	11.9	24.5
303.5	8210	6353	10332	0.398	16.3	14.9	17.8	20.2	14.1	27.0
313.5	8663	6570	10648	0.350	14.7	13.4	16.1	17.7	11.5	24.1
323.5	9112	6964	10879	0.331	14.0	12.8	15.3	16.5	10.4	22.9
333.5	9571	7319	11113	0.334	14.1	12.9	15.5	16.6	10.8	23.2
339.5	9818	7669	11226	0.335	14.1	12.9	15.5	16.8	10.9	23.4
346.5	10194	8037	11342	0.308	13.3	12.1	14.6	15.3	9.2	21.6
356.5	10701	8512	11505	0.330	14.1	12.9	15.4	16.5	10.2	22.9
366.5	11256	9713	11658	0.289	12.6	11.5	13.9	14.2	8.2	20.4
376.5	12105	11817	12913	0.292	12.8	11.7	14.0	14.4	8.2	20.5
386.5	12907	12133	13313	0.239	11.0	9.9	12.1	11.3	5.1	17.5
395.5	13673	13484	14306	0.278	12.3	11.3	13.5	13.5	7.4	19.8
401.5	14212	13611	15584	0.278	12.3	11.3	13.5	13.4	7.0	19.6

Supplementary Table 4. Pollen inferred mean summer air temperatures (JJAS) and mean annual air temperatures (MAAT) from Lower Paintrock Lake, WY and brGDGT inferred MAAT with the 25th and 75th credible intervals from Lower Paintrock Lake, WY.

Pollen-inferred			BrGDGT-inferred			
Age B.P.	JJAS °C	MAAT °C	Age B.P.	MAAT °C median	MAAT °C 25% C.I.	MAAT °C 75% C.I.
23	11.6	1.7	-59	0.1	-0.9	1.0
346	12.0	2.2	-16	-0.1	-1.0.0	0.9
665	10.7	0.7	862	1.8	0.8	2.8
1026	11.5	1.4	1200	3.9	2.9	5.1
1196	11.2	1.4	1334	1.5	0.5	2.4
1279	11.3	1.4	1477	2.7	1.7	3.7
1377	10.8	0.9	2132	2.9	1.9	4.0
1464	11.3	1.4	2375	3.2	2.2	4.4
1553	10.9	1.1	2540	4.3	3.3	5.6
2175	11.4	1.5	2782	3.4	2.5	4.5
2385	11.5	1.7	2997	3.9	2.9	5.1
2567	11.3	1.5	3703	4.2	3.1	5.4
2758	11.4	1.5	4252	3.7	2.7	4.9
2964	11.6	1.6	4584	4.4	3.3	5.7
3149	11.3	1.4	4782	4.7	3.6	5.9
3453	11.2	1.3	4988	6.3	5.1	7.9
3614	12.0	1.9	5331	5.4	4.2	6.8
3889	11.7	1.7	5522	6.2	5.0	7.7
4097	10.7	0.8	5930	3.7	2.7	4.9
4344	11.3	1.4	6207	5.8	4.7	7.3
4526	10.6	0.7	6400	4.6	3.5	5.9
4626	12.3	2.4	6879	4.4	3.3	5.6
4712	11.4	1.6	7449	6.4	5.2	8.0
4874	12.1	2.3	7919	4.9	3.8	6.2
5022	11.4	1.6	8210	6.2	5	7.7
5120	11.0	1.2	8663	4.7	3.7	6.0
5447	11.8	1.8	9112	4.1	3.1	5.5
5579	12.4	2.5	9571	4.3	3.3	5.6
5927	11.5	1.5	9818	4.3	3.3	5.6
6385	11.3	1.4	10194	3.5	2.6	4.7
6760	11.2	1.3	10701	4.2	3.1	5.5
7159	11.2	1.3	11256	3.0	2.1	4.1
7539	12.0	1.9	12105	3.1	2.2	4.2
7913	13.3	3.3	12907	1.6	0.6	2.6
8302	11.5	1.5	13673	2.7	1.8	3.8
8590	10.6	0.8	14212	2.8	1.8	3.8
8733	12.1	2.2				
8890	11.5	1.5				

Age B.P.	MAAT °C	JJAS °C
9372	12.0	2.2
9641	12.3	2.3
9975	10.7	1.0
10373	10.5	0.7
10723	10.5	0.7
11002	9.6	0.0
11147	11.0	1.4
11243	10.1	0.5
11337	10.8	0.9
11447	11.5	1.6
11581	10.9	1.1
11874	10.5	1.0
12057	11.0	1.6
12207	10.4	1.1
12354	9.6	0.3
12503	10.5	1.1
12649	10.9	1.6
12795	12.4	2.7
12942	10.2	0.8

Note: The RMSE for the pollen MAAT calibration is 1.8°C.

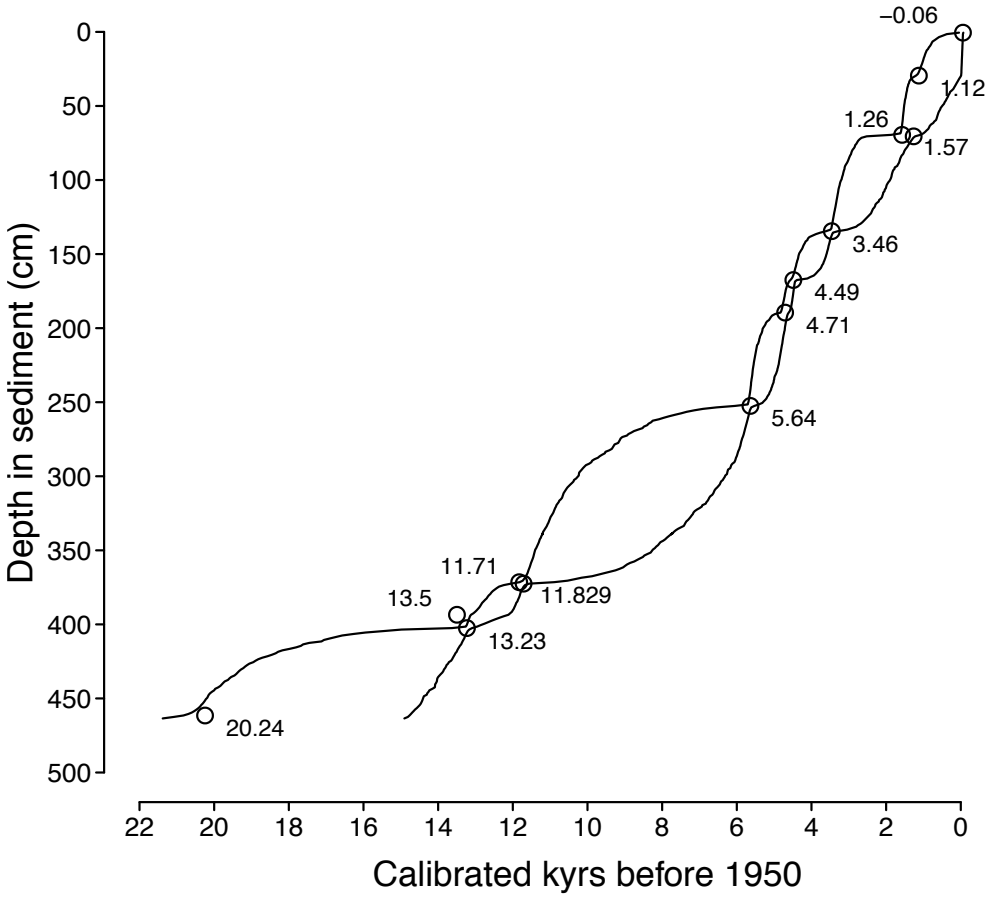

Supplementary Figure 1. Age model versus depth in sediment at Lower Paintrock Lake, WY; radiocarbon ages are shown with open circles while the black lines represent the 90th percent credible intervals of modeled ages.

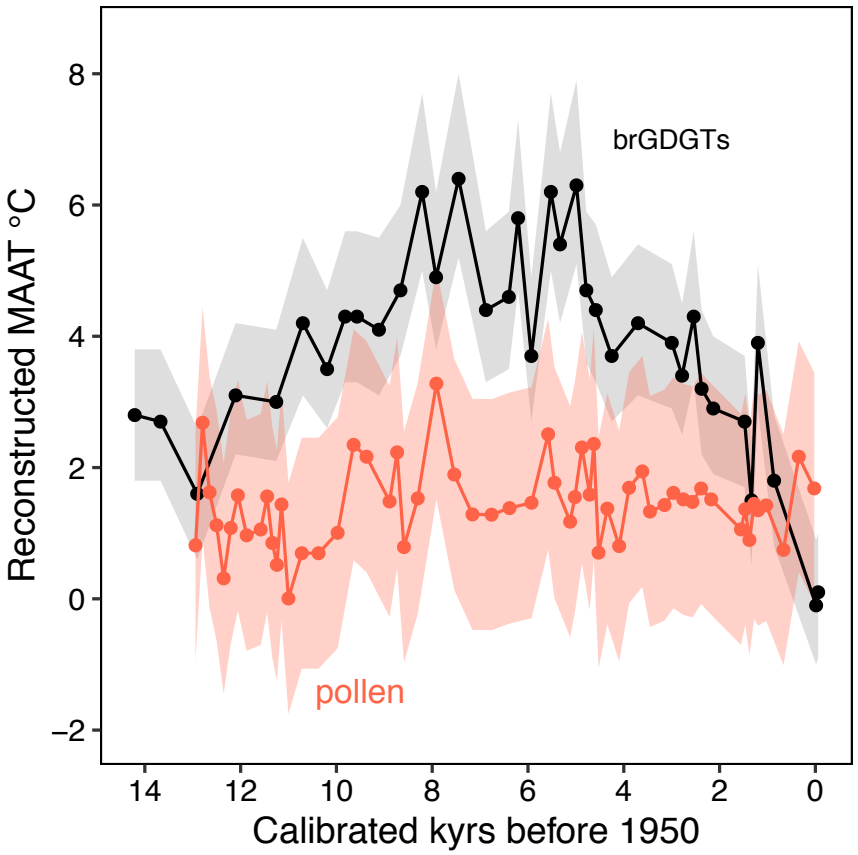

Supplementary Figure 2. Reconstructions of MAAT based on the MBT'$_{5Me}$ index (black line; grey area represents the central 50% C.I.) and pollen (orange line; light orange area represents ±RMSE) from LPR using the same methods employed in the main text. The brGDGT-based reconstructions was generated with the Bayesian calibration listed below.

Bayesian calibration for MAAT

The Bayesian calibration model for MBT'$_{5Me}$ as a function of both mean annual air temperature (MAAT) and ln(water depth) at mid-latitude, high-elevation North America is:

MBT'$_{5Me}$ = 0.031 (± 0.009) * MAAT °C - 0.058 (± 0.006) * ln(water depth in meters) + 0.32 (± 0.01)

and error σ^2=0.002 (±0.0005)

where the coefficients and their uncertainties represent the mean and one standard deviation of 4500 iterations of possible slope, intercept and error values generated by the Bayesian regression model.